Palatal segment contributions to midfacial growth in three inbred mouse strains

Short running page heading: **Palatal segment contributions to midfacial growth**

Ian C. Welsh @X – 1) Program in Craniofacial Biology, 2) Department of Orofacial Sciences and 3) Department of Anatomy, University of California at San Francisco, San Francisco, California 94143, USA

Maria E. Feiler – Interdepartmental Doctoral Program in Anthropological Sciences, Stony Brook University, Stony Brook, NY 11790

Danika Lipman @Y – Department of Cell Biology and Anatomy, University of Calgary

Isabel Mormile – Interdepartmental Doctoral Program in Anthropological Sciences, Stony Brook University, Stony Brook, NY 11790

Karissa Hansen – 1) Program in Craniofacial Biology, 2) Department of Orofacial Sciences and 3) Department of Anatomy, University of California San Francisco, San Francisco, CA 94143

Christopher J. Percival* – Department of Anthropology, Stony Brook University, Stony Brook NY 11794

* = Corresponding Author: Department of Anthropology, Circle Road, SBS Building S-501, Stony Brook, NY 11994, christopher.percival@stonybrook.edu

@X Present Address: The Jackson Laboratory, 600 Main St. Bar Harbor, ME 04609

@Y Present Address: Department of Mathematics and Statistics, 612 Campus Place NW, University of Calgary, Calgary, AB

Abstract

Following facial prominence fusion, anterior-posterior (A-P) elongation of the palate is a critical aspect of palatogenesis and integrated midfacial elongation. Reciprocal epithelial-mesenchymal interactions drive secondary palate elongation and periodic signaling center formation within the rugae growth zone (RGZ). However, the relationship between RGZ dynamics and the morphogenetic behavior of underlying palatal bone mesenchymal precursors has remained enigmatic. Our results indicate that cellular activity at the RGZ simultaneously drives rugae formation and elongation of the maxillary bone primordium within the anterior secondary palate, which more than doubles in length prior to palatal shelf fusion. The first formed palatal ruga, found just posterior to the RGZ, represents a consistent morphological boundary between anterior and posterior secondary palate bone precursors, being found at the future maxillary-palatine suture. These results suggest a model where changes in RGZ-driven A-P growth of the anterior secondary palate may produce interspecies and intraspecies differences in facial prognathism and differences in the proportional contribution of palatal segment-associated bones to total palate length. An ontogenetic comparison of three inbred mouse strains indicated that while RGZ-driven growth of the anterior secondary palate is critical for early midfacial outgrowth, subtle strain-specific bony contributions to adult palate length are not present until after this initial palatal growth period. This multifaceted illustration of normal midfacial growth dynamics confirms a one-to-one relationship between palatal segments and upper jaw bones during the earliest stages of palatal growth, which may serve as the basis for evolutionary change in upper jaw morphology. Additionally, identified mouse strain-specific differences in palatal segment elongation provide a useful foundation for understanding the impact of background genetic effects on facial morphogenesis.

Keywords: palatogenesis, secondary palate, rugae, inbred mouse strains, face elongation, RRID:IMSR_JAX:003715, RRID:IMSR_JAX:001976, RRID:IMSR_JAX:000664

Introduction

Morphological variation of the midfacial complex, which consists of the nose, upper jaw, cheek, and palate, is a defining aspect of both intra- and inter-specific differences in facial shape. Evolutionary differences in midfacial prognathism can be quantified as variation in upper jaw bone elongation and in the proportional contribution of specific bones to total upper jaw length. Species-specific differences in the size, shape, and growth trajectories of cranial neural crest (CNC)-derived facial prominences, the frontonasal process (FNP) and maxillary processes (MxP), are identifiable during the earliest phases of facial morphogenesis, prior to skeletal differentiation, often presaging interspecies differences in adult facial shape (Selleri and Rijli, 2023). Notably, after initial facial prominence fusion, early facial growth often includes substantial anterior-posterior (A-P) midfacial elongation, leading to variable degrees of midfacial prognathism (Young et al., 2014); possibly based on the balance of CNC progenitor self-renewal versus osteoblast differentiation (Hall et al., 2014; Morris and Abzhanov, 2021; Schneider, 2015). Although characteristic interspecies differences in craniofacial morphology are often present at birth (Ponce de León and Zollikofer, 2001; Zumpano and Richtsmeier, 2003; Cobb and O'Higgins, 2004; Singleton, 2012; Smith et al., 2015; Woronowicz and Schneider, 2019; Kundrát et al., 2020), postnatal bone deposition and remodeling are also required to produce the highly differentiated adult morphology, which often includes more extreme midfacial prognathism (Enlow and Bang, 1965; Sarnat, 1997; Cobb and O'Higgins, 2004; Leigh, 2006;

74 Martinez-Maza et al., 2013; Maga, 2016). Thus, both embryonic and postnatal developmental
75 processes play a role in determining adult upper jaw size and shape.
76 Basic facial shape is the result of facial prominence outgrowth and a series of fusion
77 events, which occur between embryonic day (E) 10 and E15 in mice (Fig. 1). Initial fusion
78 between the medial nasal processes (mnp) of the FNP and the anterior MxP gives rise to the
79 primary palate and lip while also producing a unified upper jaw from previously separated
80 tissues. Disproportional growth of FNP or MxP prior to fusion can result in cleft lip and palate,
81 leading to reduced evolutionary fitness. Conversely, differential growth of FNP and MxP derived
82 tissues after facial prominence fusion is a major basis for evolutionary differences in midfacial
83 elongation; where facial elongation is driven primarily by MxP growth in mammals and by FNP
84 growth in birds (Young et al., 2014).
85

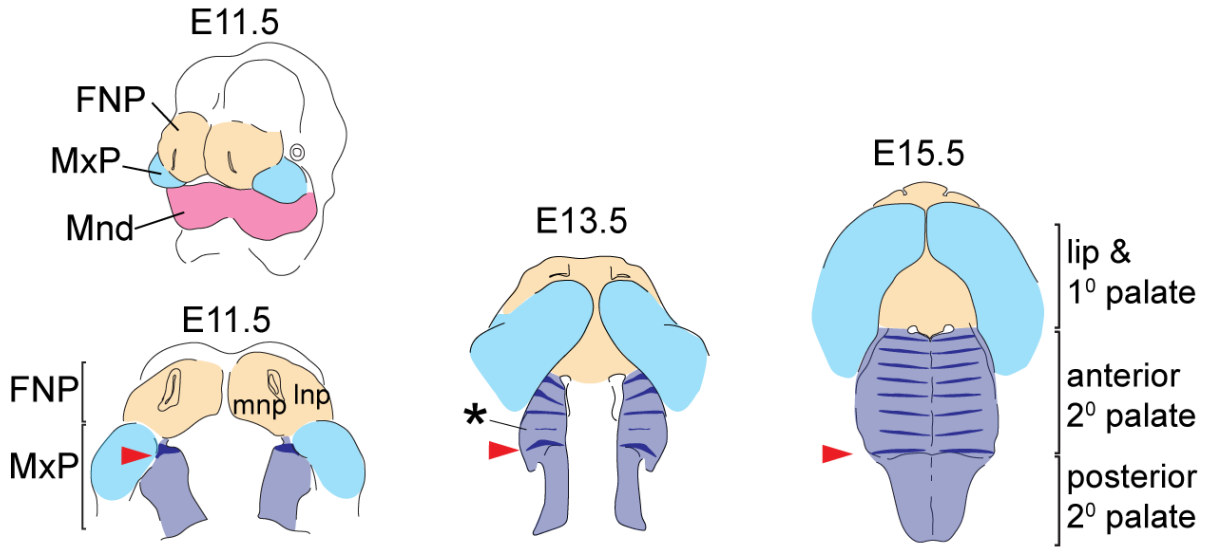

86
87 Figure 1 – Tissue origins of the midfacial complex and rugae position during secondary palate morphogenesis – The
88 upper and lower jaws are formed from the frontonasal process (FNP - tan), and branchial arch 1 derived maxillary
89 and mandibular processes (MxP - pale blue and Mnd – magenta, respectively). From E11.5 to E15.5, outgrowth and
90 fusion of the medial nasal process (mnp) with the superficial portion of the MxP frame out the lip and primary (1°)

91 palate, while the A-P elongation and medially directed growth of the palatal shelves from the internal portion of the
92 MxP gives rise to the secondary palate (2º pal – light purple). *Shh* expression (dark blue) highlights the dynamics of
93 rugae formation and illustrates regional expansion of the anterior secondary palate. At E11.5, ruga 1 (red
94 arrowheads) forms at the anterior extent of the nascent palatal shelf and subsequently defines the caudal end of the
95 rugae growth zone (asterisk) where new rugae form prior to being displaced anteriorly. Additional abbreviation:
96 lateral nasal process (lnp).
97
98 Soon after primary palate fusion at E11.5 in mice, secondary palate morphogenesis
99 begins through outgrowth of the nascent palatal shelf along the medial aspect of the MxP.
100 Significant palatal growth along the A-P axis is accompanied by vertical growth of the palatal
101 shelves prior to their elevation and medial fusion dorsal to the tongue, after which the palatal
102 shelf separates the oral and nasal cavities (Bush and Jiang, 2012; Hammond and Dixon, 2022). A
103 lack of coordination between the multiple growth axes of MxP-derived tissues can prevent
104 secondary palate closure even when the palatal shelves maintain competency to fuse.
105 The mammalian palate is composed of three major longitudinal segments called the
106 primary palate, anterior secondary palate, and posterior secondary palate. The boundary between
107 primary palate and anterior secondary palate is the posterior edge of the fused mnps. The A-P
108 organization of the secondary palate can be defined by various criteria including the presence of
109 boney versus muscular tissue (i.e. the hard versus soft palate), modes of palatal shelf elevation
110 and closure, and molecular differences in tissue patterning and cell signaling competence
111 (Hilliard et al., 2005; Yu and Ornitz, 2011; Hammond and Dixon, 2022). We use mutually
112 exclusive patterns of gene expression and the position of epithelial appendages called rugae to
113 define the boundary between anterior secondary and posterior secondary palate, as described
114 below.

115 From a morphogenetic regulatory perspective, the spatial expression of cell type specific
116 transcription factors (TFs) and intercellular signaling molecules is particularly informative to
117 understanding A-P organization of palate growth. For example, the CNC-derived mesenchymal
118 expression of *Msx1* and *Shox2* is exclusive to the anterior secondary palate during palate
119 morphogenesis, while *Barx1* and *Tbx22* expression is exclusive to the posterior secondary palate
120 (Hilliard et al., 2005; Okano et al., 2006; Welsh et al., 2018). Mutation of *Shox2* or *Tbx22* results
121 in midline clefts of the anterior or posterior palate, respectively (Yu et al., 2005; Pauws et al.,
122 2009), although normal expression of these factors is maintained in genetically engineered mice
123 with severe segmental growth defects (Welsh et al., 2018). The A-P expression boundary of
124 these and other factors is found at the first formed palatal ruga (Hilliard et al., 2005; Li and Ding,
125 2007; Welsh et al., 2007; Welsh and O'Brien, 2009; Welsh et al., 2018; Hammond and Dixon,
126 2022), one of multiple parallel epithelial thickenings on the anterior secondary palate.
127 The first ruga (ruga 1 numbered according to (Welsh et al., 2007; Welsh and O'Brien,
128 2009, although see Pantalacci et al., 2008) forms at E11.5 on the anterior extent of the nascent
129 secondary palate (Fig. 1). Remaining rugae form sequentially within the rugae growth zone
130 (RGZ) located just anterior to ruga 1 (Welsh and O'Brien, 2009), via a Turing type mechanism
131 (Economou et al., 2012; Kawasaki et al., 2018). Rugae are centers of Sonic Hedgehog signaling
132 (SHH) that is critical for anterior secondary palatal patterning and A-P growth. As the secondary
133 palate completes midline fusion at E15.5, the last formed ruga appears adjacent to ruga 1 in the
134 middle palate while each precedingly formed ruga is found at an increasingly anterior position
135 along the anterior secondary palate.
136 Based upon the dynamics of rugae formation, palate growth, and patterning gene
137 expression, Pantalacci (et al., 2008) hypothesized that ruga 1 represents a distinct morphological

138 boundary related to either the future hard versus soft palate boundary or the maxillary-palatine
139 suture. However, the dynamics of rugae formation and A-P patterns of molecular and
140 morphological variation in the secondary palate have not been explicitly defined in relation to the
141 earliest stages of facial bone development. One goal of our research was to further clarify the
142 degree to which early ontogenetic processes in the palate are coordinated with skeletal
143 differentiation. To address this knowledge gap, we defined the anatomical and molecular
144 relationship of the anterior and posterior secondary palate during anterior secondary palate
145 outgrowth with reference to boundary ruga 1, the rugae forming RGZ, and the broader context of
146 midfacial anatomical structures. We systematically mapped the initial specification and early
147 differentiation of osteoblasts relative to this anatomically defined segmental organization across
148 a developmental time course spanning mouse secondary palate morphogenesis and upper jaw
149 outgrowth (E11.5-E15.5). Visualization of molecular markers during the earliest phases of
150 palatal morphogenesis reveals the segmental origins of upper jaw bone formation and a
151 previously unappreciated coupling of maxillary formation to rugae morphogenesis during
152 expansion of the anterior secondary palate.

153 Given that 1) there is strong early one-to-one association between upper jaw bones and
154 the three major palatal segments (primary, anterior secondary, posterior secondary), 2)
155 morphogenic and differentiative dynamics are distinct along the A-P axis of the elongating
156 midface, and 3) complex embryonic processes at cellular and tissue levels are often critical for
157 the production of typical facial shape (Hilliard et al., 2005; Kaucka et al., 2018; Yuan et al.,
158 2020), early differences in the longitudinal growth of the three palatal segments might underlie
159 inter- and intraspecies differences in upper jaw morphology. Specifically, we hypothesized that
160 genetically based differences in palate segment-specific A-P outgrowth would explain previously

161 identified variation in the contribution of the premaxilla, maxilla, and palatine bones to adult
162 upper jaw morphology of inbred mouse strains (Percival et al., 2016). For example, a minor
163 segment-specific reduction in the growth rate of the anterior secondary palate between E11.5 and
164 E15.5 could result in a relatively short anterior secondary palate and relatively short adult
165 maxillary bone, as identified within the C57BL/6J (C57; RRID:IMSR_JAX:000664) strain.
166 To test our hypothesis and shed light on the overall developmental basis of adult palatal
167 morphology, we measured the facial morphology of an ontogenetic series of common inbred
168 strains of mice between E11 and E15, one day after birth, and in adults (8-12 weeks old). The
169 C57 and NOD/ShiLtJ (NOD; RRID:IMSR_JAX:001976) inbred strains were chosen because
170 C57 adults have a relatively long premaxilla and NOD adults have a relatively long maxilla
171 (Percival et al., 2016). The PWK/PhJ (PWK; RRID:IMSR_JAX:003715) wild-derived inbred
172 strain was chosen as a mouse with a smaller adult body size, a relatively long maxilla compared
173 to the premaxilla, and a relatively long upper jaw for its body size when compared to the other
174 strains (Percival et al., 2016). If variation in early A-P elongation of longitudinal palatal shelf
175 segments is the causal basis for strain specific differences in upper jaw morphology, we
176 predicted that C57 mice would have a relatively long primary palate and a relatively short
177 anterior secondary palate by E15 and that the other two strains would display relatively long
178 anterior secondary palates at the same developmental stage.
179 Understanding how genetically based differences in early craniofacial development
180 produce morphological variation within model organisms is an important step in determining
181 how these developmental processes can be modified to produce evolutionary differences in upper
182 jaw morphology (Boughner et al., 2008; Hallgrímsson et al., 2009; Fish, 2019; Morris and
183 Abzhanov, 2021), including facial length and the relative contribution of specific bones to the

upper jaw. The subtle strain-associated differences in palatal morphology we report are reminiscent of brachycephalic versus dolichocephalic dog breeds and species-level differences between primates, including the reduced facial length of humans compared to other apes and the increased facial length of baboons compared to other cercopithecines. Overall, our multifaceted analysis of ontogenetic trends in palatal and facial elongation provides a novel contextual framework and developmental perspective within which to evaluate the impact of both non-pathogenic as well as pathogenic genetic differences on midfacial growth and differentiation.

Methods

Specimen and Image Acquisition

Animal breeding, specimen collection, and tissue fixation were performed in accordance with the protocols of the University of California, San Francisco Institutional Animal Care and Use Committee under protocol approval number AN192776-01F. Mice were socially housed under a twelve-hour light-dark cycle with food and water *ad libitum*. Additional enrichment was provided when single housing was required for breeding purposes. Mice were euthanized by CO_2 inhalation followed by cervical dislocation or decapitation. Embryos of C57BL/6J (RRID:IMSR_JAX:000664; C57), NOD/ShiLtJ (RRID:IMSR_JAX:001976; NOD), and PWK/PhJ (RRID:IMSR_JAX:003715; PWK) strains (Jackson Labs, Bar Harbor, ME) were collected between gestational days E11.5 and E15.5, as determined from copulatory plug occurrence. Postnatal day one (P1) C57 (n=10) and NOD (n=7) specimens were collected one day after birth. Embryo and P1 specimens were fixed in 4% PFA and stored in 1x PBS for micro-computed tomography (μCT) imaging or dehydrated through a graded PBST-MeOH series and stored at -20°C until use for in situ hybridization.

207 Specimens for µCT scanning were received, stored, and imaged at the University of
208 Calgary in accordance with the protocols of the University of Calgary Institutional Care and Use
209 Committee under approval number AC13-0268. After approximately an hour of soaking in
210 Cysto-Conray II (Liebel-Flarsheim Canada), µCT images of embryo heads were acquired with a
211 Scanco µ35 with 45kV/177µA for images of 0.012 mm^3 voxel size. µCT images of P1 heads
212 were acquired similarly, but with 0.021 mm^3 voxel size. Photographs of embryo hindlimb buds
213 were collected using a dissecting microscope for developmental age estimation. Adult specimens
214 were previously collected and µCT imaged, as described by Percival et al., 2016.
215
216 **In Situ Hybridization**
217 In situ hybridization was performed as described in Welsh et al., 2018. cDNA probes for
218 *Phospho1* (nucleotides 274–1739 of RefSeq NM_153104), *Runx2* (nucleotides 1275–2704 of
219 RefSeq NM_001271627), *Shh* (full length cDNA clone from A. McMahon, University of
220 Southern California, Los Angeles CA, USA), *Shox2* (nucleotides 870–1603 of RefSeq
221 NM_130458), *Sp7* (nucleotides 431–1715 of RefSeq NM_130458), *Tbx22* (nucleotides 307–
222 1547 of RefSeq NM_013665) were linearized and in vitro transcribed to label with either
223 digoxygenin (DIG) or dintrophenol (DNP). Colorimetric detection of probes used BM purple
224 (dark blue), BCIP (teal), or MagentaPhos (magenta).
225
226 **DMDD HREM Data**
227 High resolution episcopic microscopy (HREM) data (Geyer et al., 2009) was generated as
228 part of the deciphering mechanisms of developmental disorders (DMDD) program (Wilson et al.,

229 2016) and is available from the BioImage Archive at:

230 https://www.ebi.ac.uk/biostudies/bioimages/studies/S-BIAD490?query=DMDD

231

232 **Embryonic Palatal Segment Growth Trajectories**

233 Developmental Age Estimation

234 Given that common mouse strains vary in gestation length and there is variation in

235 developmental timing within litters, it was necessary to standardize our cross-strain

236 morphometric analysis by embryonic developmental age rather than gestational age.

237 Developmental age was estimated for each µCT scanned embryonic specimen using eMOSS, an

238 application that predicts developmental age from hindlimb bud outlines, based on a previous

239 analysis of C57 mice (Musy et al., 2018). The resulting limb-based estimates of developmental

240 age were reported as days since conception, up to two decimal places. We combined similar

241 developmental age estimates into developmental age categories so that specimens were assigned

242 to a whole- or half-day developmental age within 0.25 days of their initial eMOSS estimate

243 (Table 1). For example, an eMOSS estimated E12.20 specimen was assigned to the E12.0 limb-

244 based developmental age category.

245

246

247 Table 1 –Sample size of µCT imaged and morphometrically analyzed embryo specimens by strain and
248 forelimb based developmental age estimation, as estimated using eMOSS (Musy et al., 2018).

Limb-Based Developmental Age	C57	NOD	PWK
E11	8	12	4
E11.5	2	0	0
E12	7	3	6
E12.5	4	0	2
E13	9	3	6
E13.5	0	0	2
E14	26	6	6
E14.5	1	0	0
E15	9	4	0

249

250

251 Additional error may be expected when estimating the developmental age of NOD and
252 PWK embryos using a predictive model built on C57 strain limb bud ontogeny, given the
253 possibility of differences in the correlation of limb and head development between strains.
254 Therefore, we also utilized the first principal component of embryonic head shape variation
255 (PC1), based on the landmark analysis described below, as a proxy for developmental age in
256 some analyses. PC1 score consistently tracked ontogenetic change in facial and palatal shape
257 across strains (see Results).

258

259 Anatomical Landmark Collection

260 All embryo facial and palate landmarks were collected within Meshlab (Cignoni et al.,
261 2008) on minimum threshold-based superficial tissue surfaces (downsampled x2) produced from
262 the µCT images. Landmarks that could be identified consistently in anatomically homologous
263 positions across the embryonic period of facial growth were chosen around the nose and whisker

region, the eyes, and along the palate (Fig. 2, Supporting Table 1). Care was taken to define epithelial tissue palatal landmarks in embryos that could be associated with the bony morphology of the P1 and adult mouse upper jaw.

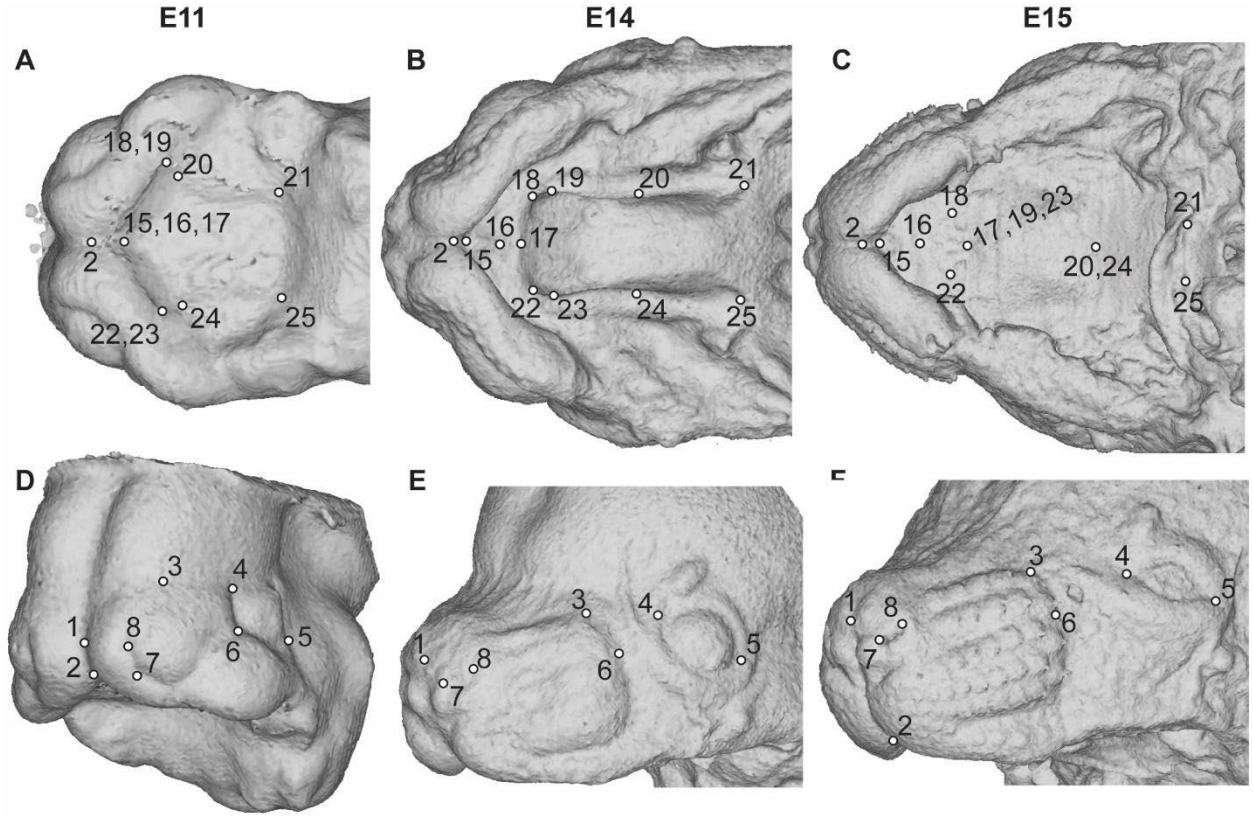

Figure 2 – Anatomically homologous epithelial landmarks collected for the quantification of midfacial and palatal shape across limb based developmental stages, from (a-c) palatal and (d-f) oblique facial views. See also Supporting Table 1.

Prenatal Geometric Morphometric Analysis

A Procrustes superimposition-based geometric morphometric analysis was used to quantify the ontogenetic shape change of the palate and face for the embryonic C57 sample and deviations of the NOD and PWK strains from this C57 baseline. Embryonic specimens with limb-based developmental age estimates between E11 and E15 were included in the embryonic

shape analysis (Table 1). We performed a geometric morphometric analysis of facial landmarks using *geomorph* (Adams et al., 2020) and RRPP (Collyer and Adams, 2018) libraries in R Statistical Software (R Core Team, 2021). We first performed a generalized Procrustes analysis (GPA) to align specimen landmark sets by translating, scaling, and rotating their landmark coordinates (reviewed by Zelditch et al., 2012). Embryonic specimen shape analyses were completed using the symmetric component of Procrustes-aligned specimen landmark coordinate variation, as we assumed that most bilateral shape differences between the left and right sides of a specimen's face are due to random effects associated with developmental noise and tissue fixation (Palmer and Strobeck, 1986). Thus, symmetrized landmark coordinate data were interpreted to represent the facial shape defined by a given inbred strain genotype.

The mean facial shape of specimens within each developmental age category were estimated for each strain. Differences between the mean shapes of a subset of developmental age categories within the C57 sample were plotted to illustrate typical facial/palatal shape growth trajectories during this important period of secondary palate elongation and midline fusion.

A principal components analysis (PCA) was completed to identify the major axes of shape covariation across the embryonic sample. As with most PCA of ontogenetic series, the first principal component (PC1) was strongly associated with overall specimen size and specimen developmental age. Therefore, we treated it as a proxy for ontogenetic growth and developmental age. C57-specific segmented linear regressions represented a baseline of overall facial/palatal shape change to which the NOD and PWK specimens were compared. Due to clear inflection points in the slopes of embryonic specimen PC scores when plotted against PC1, segmented linear regressions were completed separately for PC2, PC3, and PC4 versus PC1 values for the C57 sample.

300 After removing three NOD specimens with PC1 scores that were substantially lower than
301 the minimum C57 PC1 score that the C57 regression was based on, we predicted PC2, PC3, and
302 PC4 scores from each C57, NOD, and PWK specimen's PC1 score based on the C57 baseline
303 segmented regressions. Then we calculated the PC score residuals of each specimen as the
304 difference between predicted and measured PC scores. We completed Wilcoxon rank sum tests
305 to identify significant genotypic differences for PC2, PC3, and PC4 residual values. A significant
306 difference in mean PC score residual values between strains was interpreted as a significant
307 difference in the ontogeny of facial shape for that pair of strains.
308
309 Prenatal Palate Segment Length
310 The anterior-posterior length of the three major palatal segments (i.e., primary palate,
311 anterior secondary palate, and posterior secondary palate) were estimated from landmark
312 coordinates without any superimposition or scaling. To estimate the length of these segments
313 along the anterior-posterior axis of the palate, the mean position of bilateral pairs of palatal
314 landmarks were calculated (i.e., the midline projection of the bilateral landmarks). Primary
315 palate, anterior secondary palate, and posterior secondary palate lengths were calculated in
316 millimeters from these landmark positions. Proportional palatal segment lengths were calculated
317 as the length of a single segment divided by the sum of all three segment lengths for a given
318 specimen. LM15 represented the midline anterior extent of the primary palate, the midpoint
319 between LM18 and LM22 represented the border between primary palate and the anterior
320 secondary palate, the midpoint between LM20 and LM24 represented the border between the
321 anterior and posterior secondary palate, the midpoint between LM21 and LM25 represented the
322 posterior boundary of the posterior secondary palate.

323 Small strain-specific sample sizes at multiple limb-based developmental ages meant it
324 was not possible to statistically test whether the genetic strains had different proportional palatal
325 segment contributions at single developmental ages. Instead, separate second-degree polynomial
326 regressions of proportional palate segment lengths versus specimen facial shape PC1 score were
327 calculated for the C57 embryos. Because PC1 score was considered a proxy for developmental
328 age, these regressions define ontogenetic trajectories of palatal segment contributions to overall
329 palatal length, which we used as a baseline for comparison with NOD and PWK proportional
330 segment lengths. After removing three NOD specimens with PC1 scores that were substantially
331 lower than the minimum C57 PC1 score, we predicted the proportional length of each palatal
332 segment for all specimens based on the C57 regressions. The residual differences in proportional
333 palatal segment lengths between predicted and measured values were compared across the three
334 strains using Wilcoxon rank sum tests. A significant difference in mean residual values was
335 interpreted to indicate a generally higher or lower proportional contribution of a given palate
336 segment to overall palatal length across the embryonic period being measured.
337
338 **Postnatal Palate Segment Length Comparisons**
339 To determine if embryonic differences in proportional palate segment length remained
340 consistent postnatally and to investigate the degree of correspondence between surface epithelial
341 and skeletal measures of palatal variation, postnatal specimen landmarks were collected on
342 minimum threshold-based surfaces produced from μCT scans. Superficial epithelial surfaces of
343 P1 specimens were produced using Amira (downsampled x2), and epithelial landmarks
344 (Supporting Table 1) were collected within Meshlab (Cignoni et al., 2008).

345 Minimum threshold-based skeletal surfaces of P1 and adult specimens were produced
346 using 3D Slicer (Fedorov et al., 2012) after Gaussian blur image filtering (sigma set to 0.01 for
347 P1; sigma set to 0.02 for adult). We identified skeletal anatomical landmarks that most closely
348 matched the palate segment landmarks defined on surface epithelium (Supporting Table 2).
349 Landmarks were collected for C57 (n=10) and NOD (n=8) P1 specimens and for C57 (n=20),
350 NOD (n=18), and PWK (n=18) adult specimens. Midline palate segment lengths and associated
351 upper jaw bone lengths were measured using landmark coordinates without scaling or
352 superimposition. Midline points were calculated from pairs of bilateral landmarks defining each
353 palate segment boundary, midline projected palate segment lengths were estimated for each
354 specimen, and total palate length was calculated as the sum of the three midline palate segment
355 lengths. Proportional palate segment lengths were calculated as individual segment lengths
356 divided by total palate length. Wilcoxon rank sum tests were used to identify significant
357 differences in proportional palate segment lengths between strains within single age and tissue
358 type categories.
359

360 **Results**

361 **Defining an Anatomical and Molecular Reference Framework of Secondary Palate A-P**
362 **Growth**

363 We defined the anatomical relationship between the boundary ruga 1, the surrounding
364 midfacial anatomy, and the A-P expression of genes critical for palatal shelf patterning as a
365 foundation for assessing rugae morphogenesis and segmental growth dynamics of the secondary
366 palate. A-P secondary palate elongation was defined with reference to the first ruga's position at
367 the boundary between the anterior and posterior secondary palate and the A-P expression of

genes critical for palatal shelf patterning, including *Shox2* and *Tbx22*. Ruga 1 formed within the MxP at the anterior extreme of the nascent secondary palate (Fig. 3, red arrowheads). Expression of *Shox2* overlapped the medial portion of the *Shh* expression domain in forming ruga 1, while *Tbx22* palatal shelf expression was found just posterior to ruga 1. Sequential rugae formation occurred anterior to ruga 1 within the RGZ and accompanied expansion of the anterior secondary palate. *Shox2* expression remained restricted to the rugae-bearing anterior secondary palate, while *Tbx22* expression was restricted posterior to ruga 1 throughout this critical period of secondary palate elongation (Fig. 3a,c,e).

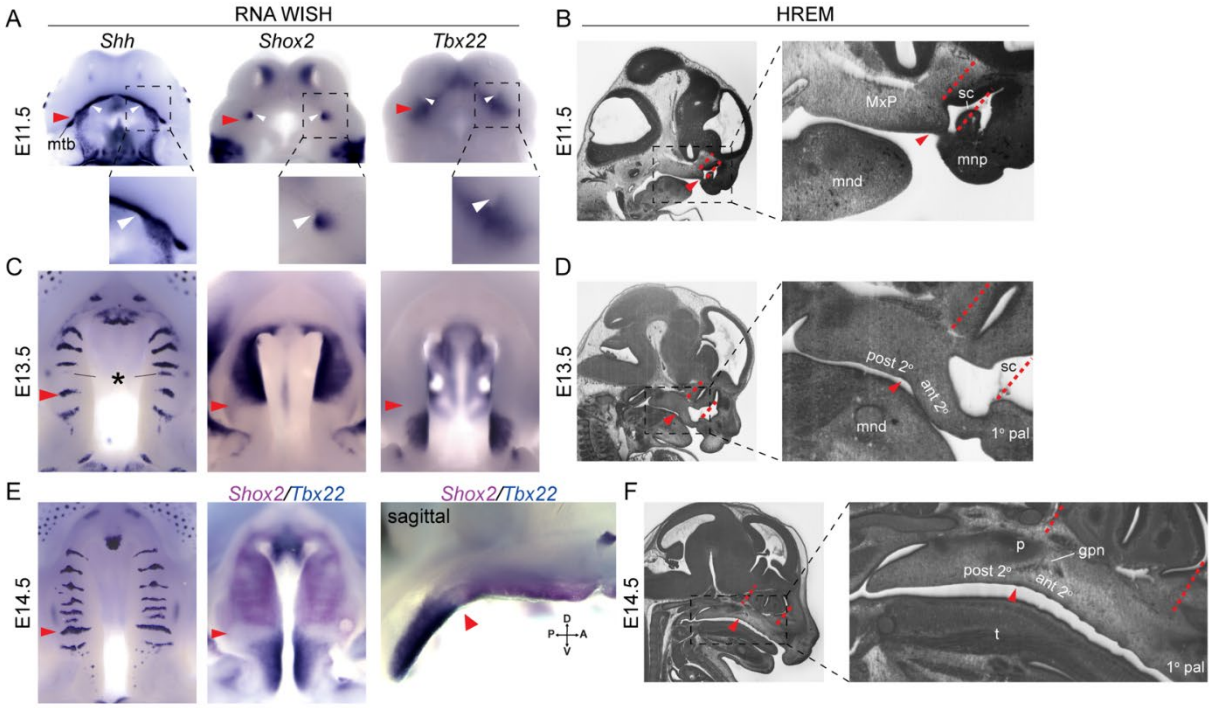

Figure 3 – A-P molecular heterogeneity and anatomical relationships during secondary palate morphogenesis. (a, c, e) Whole mount in situ hybridization for *Shh*, *Shox2*, and *Tbx22* expression, and (b, d, f) sagittal sections of wildtype embryos imaged with high resolution episcopic microscopy to provide histological resolution of the primary (1° pal), anterior secondary (ant 2°), and posterior secondary palate (post 2°) relative to surrounding facial structure during midfacial outgrowth at (a, b) E11.5 (c, d) E13.5, and (e, f) E14.5. Throughout midfacial outgrowth, ruga 1 (red arrowheads) marks the shared A-P expression boundary of *Shox2* and *Tbx22* in the anterior and posterior

383 secondary palate, respectively. Double label WISH for *Shox2* (magenta) and *Tbx22* (blue) at E14.5 highlights
384 mutually exclusive anterior and posterior expression domains organized relative to ruga 1 (oral view left, sagittal
385 view right). White arrowheads mark the choanae, black asterisk marks the RGZ. Red dashed lines mark the primary-
386 secondary palate junction and posterior wall of the nasal capsule to highlight coordinated elongation of the anterior
387 secondary palate and overlying sinus cavity (sc). Regions in dashed boxes of HREM images shown enlarged to the
388 right. Additional abbreviations: mandible (mnd), molar tooth bud (mtb), maxillary process (MxP), medial nasal
389 process (mnp), tongue (t), greater palatine nerve (gpn), palatine (p).
390
391 Close relationships between different anatomical domains underlying midfacial
392 outgrowth are found centered at ruga 1, which is at the boundary between the anterior and
393 posterior secondary palate. Elongation of the anterior secondary palate is coordinated with the
394 formation of the overlying sinus cavity, and disrupted morphogenesis of either structure can
395 impact the other (Pauws et al., 2009; Kaucka et al., 2018; Welsh et al., 2018). We found that
396 ruga 1 formed adjacent to the choanae, the posterior openings of the forming sinus cavity (Fig.
397 3a, white arrowheads). Expansion of the secondary palate anterior to ruga 1 between E11.5 and
398 E15.5 anteriorly displaced the primary palate and external nares. Ruga 1 and the posterior wall of
399 the nasal capsule remained approximately in the same coronal plane during elongation of the
400 anterior secondary palate and nasal capsule (Fig.3b,d,f), suggesting that they are positioned at a
401 proximal source of directional growth. Ruga 1 was also coincident with a gross morphological
402 inflection point of the palatal tissue where the anterior secondary palate and overlying sinus
403 cavity exhibited a more inferiorly accentuated angle relative to the cranial base than the posterior
404 secondary palate did (Fig. 3d-e, Supporting Fig. 1). Lastly, between E12.0 and E12.5, the greater
405 palatine nerve and artery were found entering the palatal shelves from a location immediately
406 dorsal to ruga 1. This spatial relationship was maintained until the greater palatine foramen
407 forms prior to E15.5 by the articulation of maxilla and palatine bones (Fig. 3f, Supporting Fig.

1). These anatomical relationships collectively demonstrated that ruga 1 represents an important stable anatomical boundary and point of reference within the context of early midfacial outgrowth and segmental organization of the palate.

We conducted a complementary 3D morphometric analysis of epithelial landmarks across the midface, including several defined by the palatal anatomy described above, to quantify the integrated morphogenetic processes occurring across the facial region during this critical early developmental period. The first major principal axis of facial shape variation (PC1) for all limb bud staged E11-E15 specimens represented the majority of shape variance present in the sample (70%) and was associated with general ontogenetic growth during this time window, as illustrated for the C57 sample (Fig. 4) and for all three inbred strains (Supporting Fig. 2). Additional principal axes of variation suggested shifts in the direction of ontogenetic shape changes over developmental time. For example, the PC2 scores of C57 embryos increased from E11 to E12.5, but then decreased again from E12.5 to E15 (Fig. 4a). The direction of shape change shifted twice along PC3 (Fig. 4b) and three times along PC4 (Fig. 4c).

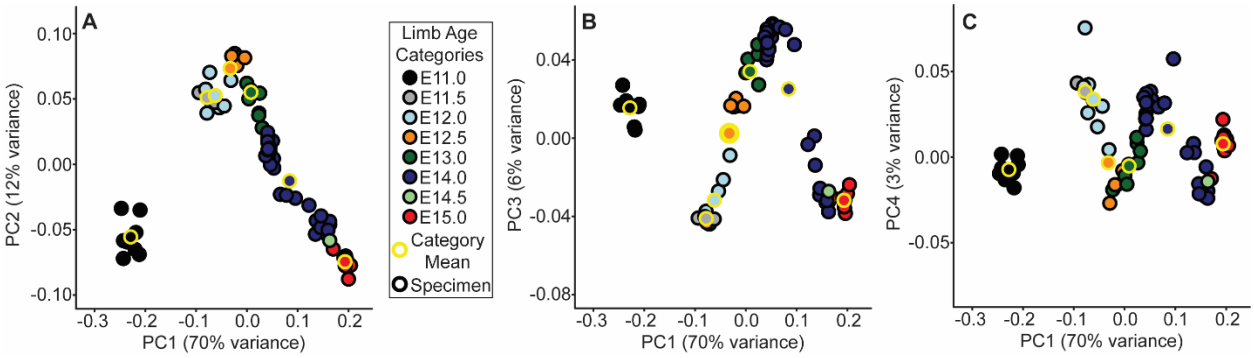

Figure 4 – Major axes of embryonic facial shape variation - C57 embryo specimens plotted along the (a) first and second principal component axes of shape (i.e., PC1 and PC2), (b) along PC1 and PC3, and (c) along PC1 and PC4. Circle color indicates the limb based developmental age categories of each specimen, with the yellow bordered circles indicating the mean PC scores for the C57 mice of that age category. The proportions of facial shape variance associated with each principal component are provided. The principal component axes were estimated from the full

428 sample of E11-E15 developmental age embryos, including C57, NOD, and PWK samples, although only C57
429 samples are plotted in this figure. The same plot, but incorporating all three inbred strains is available as Supporting
430 Figure 2.
431
432 Average developmental age category shape differences were illustrated as landmark
433 specific ontogenetic shifts in palate shape (Fig. 5) and overall midfacial shape (Supporting Fig.
434 3). Mouse embryos grew substantially between limb-based developmental ages E11 and E15,
435 including increased facial size and oral cavity length. Within C57 mice at E11, the mnp and the
436 MxP fused to create the primary palate, while the cell populations that will give rise to the
437 posterior secondary palate were already visible. Compared to E11, E12.5 specimens had a
438 relatively longer primary palate and a relatively short distance between the left and right
439 secondary palatal shelves. After E12.5, secondary palate length (relative to overall facial size)
440 increased noticeably with each developmental stage. As the specimens approached E15, the most
441 substantial changes in palatal shape were related to 1) the previously described A-P elongation of
442 the secondary palate and 2) the medial growth and ultimate fusion of the palatal shelves.

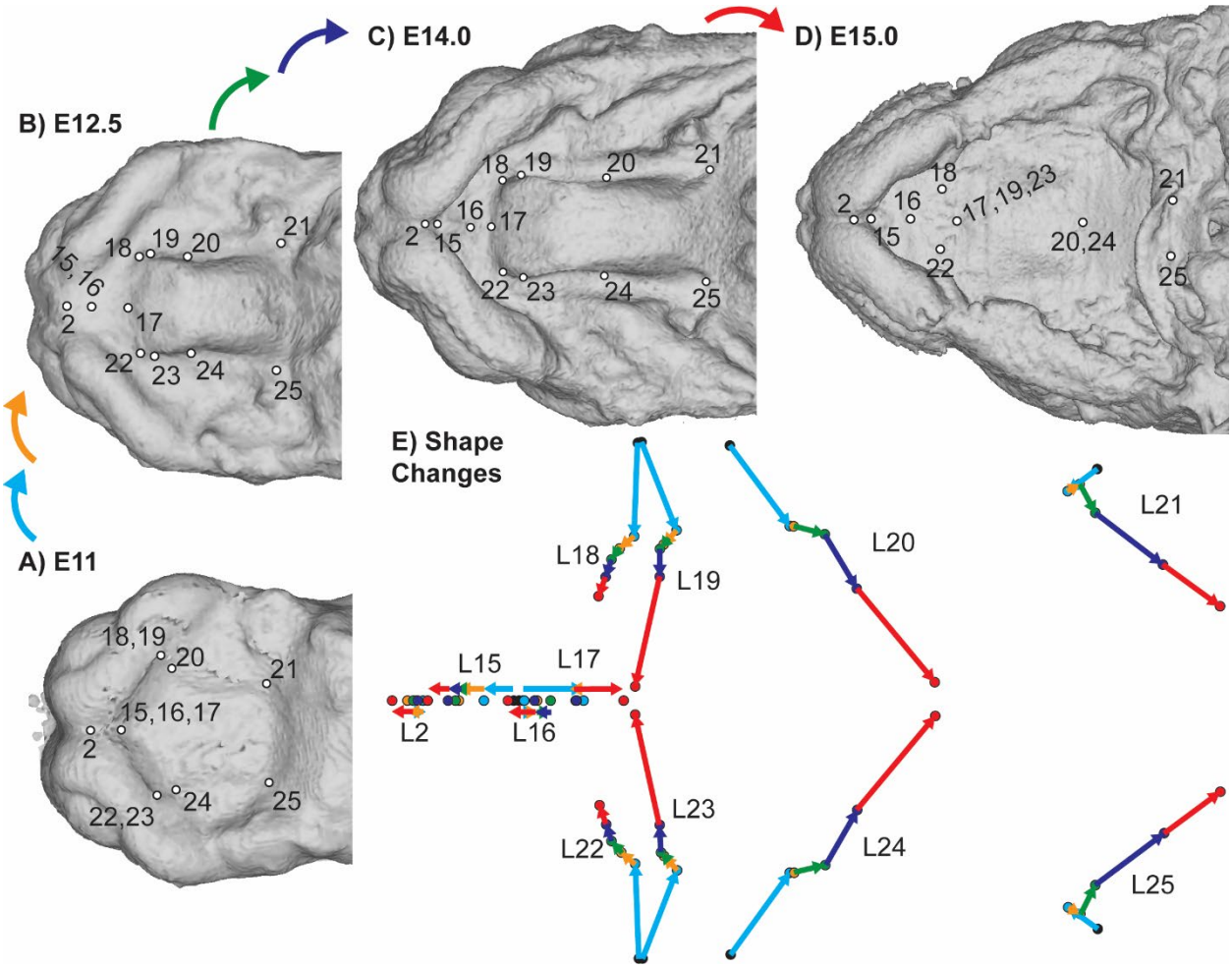

Figure 5 – C57 palatal landmark growth trajectories – The positions of palatal landmarks are identified on representative C57 specimens at limb-derived developmental ages (a) E11, (b) E12.5, (c) E14, and (d) E15. (e) The average palatal landmark positions are plotted for each developmental age category that had more than one C57 specimen. These landmark positions represent palatal shape after the removal of overall facial scale. The arrows indicate the trajectory of shape change for each landmark between ages. Black=E11; Light Blue = E12; Orange = E12.5; Green = E13; Dark Blue = E14; Red = E15.

Between developmental stages E11 and E15, each of the three major palatal segments grew in length, but the anterior secondary palate grew proportionally more than the primary palate and posterior secondary palate (Figs. 3 & 5). Midline epithelial measurements of C57 embryos soon after the start of A-P palatal elongation indicated that the primary palate

455 represented ~20% of the total palate length, the anterior secondary palate ~20%, and the
456 posterior secondary palate ~60%. In contrast, by the time of midline palatal fusion at E15.5, the
457 primary palate represented ~25% of palate length, the anterior secondary palate represented
458 >40%, while the posterior secondary palate represented <35%. Therefore, between E11 and E15,
459 the proportional contribution of the primary palate increased by a quarter, while posterior
460 secondary palate contribution decreased by nearly a third. Strikingly, the proportional
461 contribution of the anterior secondary palate doubled during this period.
462

463 **Segmental Differences in Skeletal Specification, Differentiation, and Growth During**
464 **Secondary Palate Morphogenesis**

465 Cellular changes in gene expression represent one of the most proximal steps in the
466 morphogenetic cascade of osteogenic differentiation and bone formation. We therefore sought to
467 evaluate the earliest stages of midfacial skeleton specification and differentiation in relation to
468 the pattern of segmental growth described above. We analyzed the expression of *Runx2*, *Sp7*, and
469 *Phospho1* using whole mount in situ hybridization (WISH) on mouse embryos from E11.5 to
470 E15.5, a developmental time course spanning the emergence of the secondary palate until
471 midline palatal shelf fusion. These molecular markers were chosen because *Runx2* expression
472 overlaps the initial specification of osteoprogenitors during intramembranous bone formation;
473 subsequent expression of *Sp7* is required for osteoblast precursor differentiation (Galea et al.,
474 2021; Hojo and Ohba, 2022); and the phosphatase *Phospho1* is essential for inorganic phosphate
475 incorporation and mineral deposition in the forming osteoid of differentiating osteoblasts (Dillon
476 et al., 2019).

Comparing the spatial expression dynamics for these marker genes showed that while *Runx2* signal does highlight some osteogenic domains, particularly in the premaxilla within the primary palate, it tended to be more broadly expressed within the early facial prominences. Within the developing secondary palate, expression of *Runx2* remained medial throughout this period, being restricted to domains adjacent to the molar tooth bud and medially along the adjoining palatal shelves (Fig. 6a).

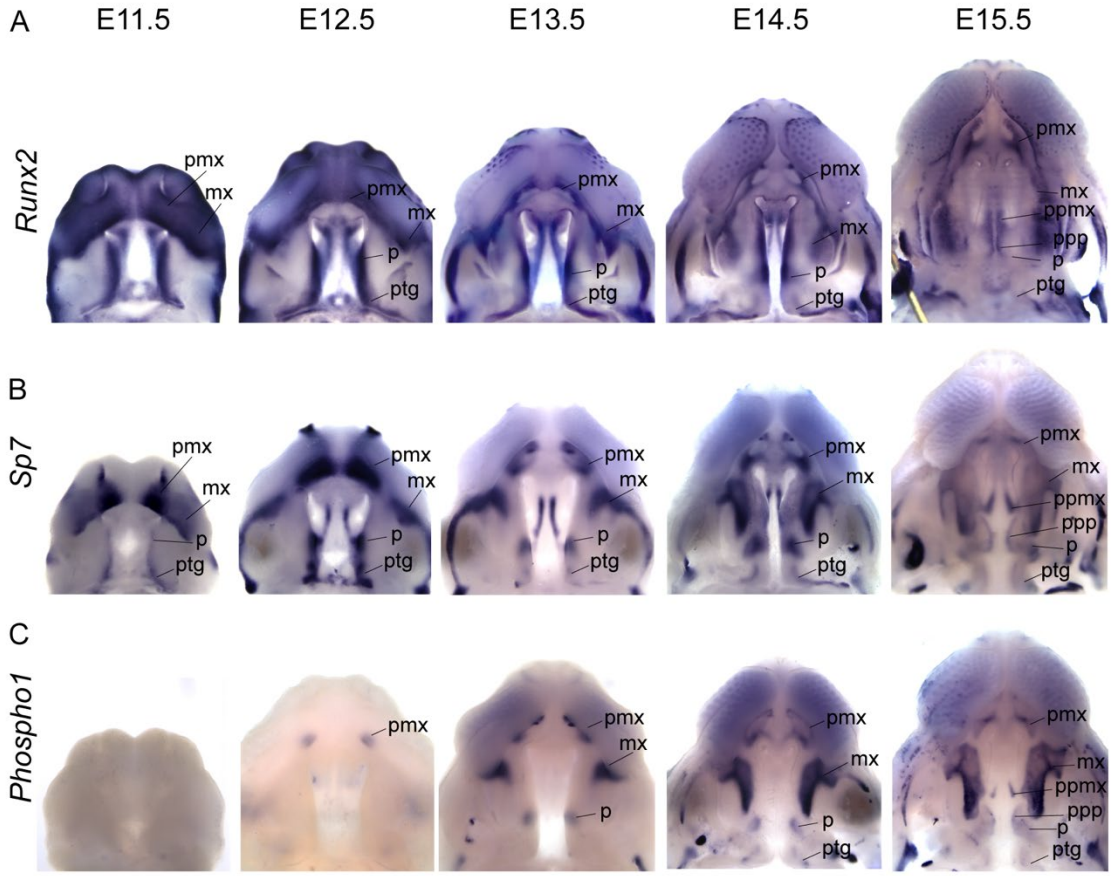

Figure 6 – Segmental organization of skeletal specification and growth during A-P morphogenesis of the midface – WISH time course for (a) *Runx2*, (b) *Sp7*, and (c) *Phospho1* between E11.5 and E15.5. Expression of *Runx2* in osteoprogenitors highlights facial domains with osteogenic potential during midfacial morphogenesis. Expression of *Sp7* and *Phospho1* in committed and differentiating osteoblasts delineates the growth dynamics of individual skeletal anlagen during midfacial morphogenesis. Abbreviations: maxilla (mx), palatine (p), premaxilla (pmx), pterygoid (ptg), palatal process of the maxilla (ppmx), palatal process of the palatine (ppp)

490

491 The osteoblast-specific expression of both *Sp7* and *Phospho1* more precisely delineated
492 the morphology of the emerging midfacial skeleton during this early period of midfacial
493 outgrowth. At E11.5, *Sp7* was strongly expressed in bilateral domains within the mnp of the
494 forming primary palate. Between E12.5 and E15.5, presaging premaxilla morphology, *Sp7*
495 expression formed a cup-like region surrounding the developing incisors (Fig. 6b). At E11.5, *Sp7*
496 expression in the MxP was observed in two domains. The anterio-lateral domain, interpreted as
497 the presumptive maxilla, abutted the point of fusion with the mnp and extended laterally away
498 from the oral cavity and choanae. The posterior domain spanned the length of the forming
499 secondary palate, from the anterior limit abutting the choanae to the posterior-most palatal edge,
500 and likely comprised the presumptive palatine and pterygoid bones. The antero-lateral domain of
501 *Sp7* maintained proximity to the primary palate throughout the growth period, formed a new
502 medial expansion (E12.5-E13.5) that extended posteriorly (E13.5-E15.5) within the growing
503 anterior secondary palate (Fig. 6b). Between E12.5 and E15.5, anterior secondary palate
504 elongation displaced the original posterior *Sp7* domain away from the primary palate. This
505 posterior domain separated into two subdomains; the anterior subdomain remained associated
506 with the posterior wall of the sinus cavity and gave rise to the palatine bone, while the posterior
507 subdomain formed the pterygoid. Likely reflecting a temporal lag between initial osteoblast
508 commitment and later differentiation, *Phospho1* was not detected in the midface at E11.5 and
509 was observed only in the forming premaxilla at E12.5, followed by expression in progressively
510 more posterior bone anlagen between E13.5 and E15.5 (Fig 6c).

511 These osteoblast-specific expression patterns indicated that the premaxilla, palatine, and
512 pterygoid anlagen grew to acquire their characteristic adult morphology within the same domains

513 where they were initially specified. However, the maxillary anlage was initially specified
514 external to the oral cavity at the site of the future zygomatic plate. Only after anterior secondary
515 palate elongation was initiated (E11.5-12.5) does a new portion of the maxillary anlage grow
516 medially into the anterior secondary palate (E12.5-13.5) and extend posteriorly towards the
517 palatine bone anlage (E13.5-15.5). The fact that *Phospho1* expression closely followed *Sp7*
518 spatial dynamics within the maxillary anlage further supported the idea that *Sp7* expression
519 patterns represent bone anlagen formation and expansion. Lastly, it is notable that the palatal
520 processes of the maxilla and palatine bones formed within the medial region of the elevated
521 palatal shelves, a domain that maintained high levels of *Runx2* expression during secondary
522 palate growth (Fig. 6a), suggesting maintenance of a less differentiated osteoprogenitor
523 population until palatal fusion was complete.
524 Rugae morphogenesis provided a set of temporally ordered anatomical features that can
525 be used to visualize A-P growth dynamics of the secondary palate. WISH double labeling of *Shh*
526 and *Sp7* between E12.5 and E15.5 indicated the position of specific rugae relative to developing
527 bone anlagen (Fig. 7a). These data further demonstrated that the initial site of maxillary
528 specification (i.e. the future zygomatic plate) maintained a position external to the oral cavity and
529 adjacent to the anterior most rugae during secondary palate elongation (Fig. 7a). Notably, medial
530 maxillary anlage expansion into the secondary palate occurred around E13.5, after initial A-P
531 growth of the anterior secondary palate and formation of 3-4 rugae anterior to ruga 1, and thus
532 uniquely coupled to RGZ growth dynamics. The maxillary anlage grew posteriorly towards ruga
533 1 and the palatine anlage at the same time as subsequent rugae formation (E13.5-E14.5; Fig. 7a).
534

Figure 7.

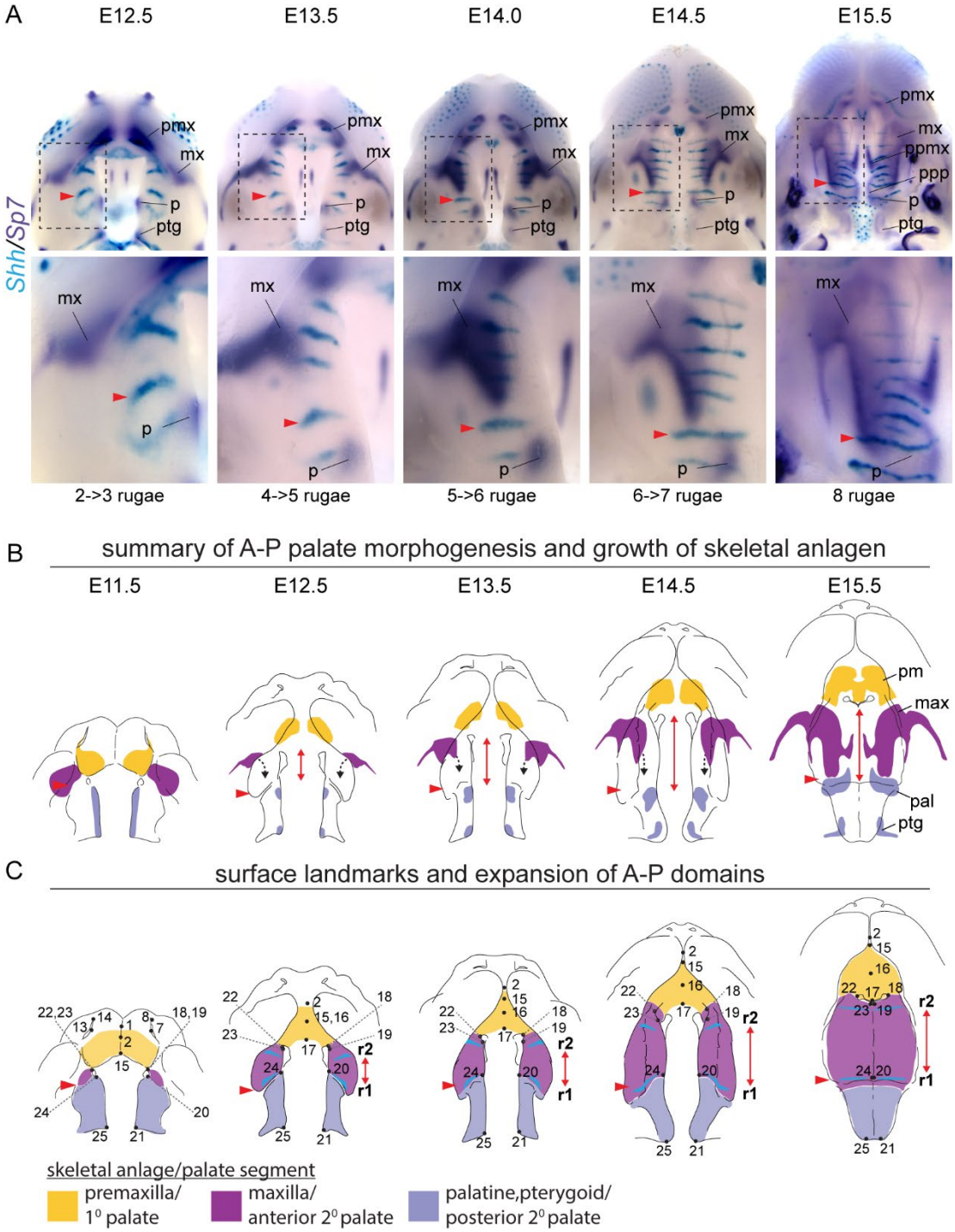

Figure 7 – Double label RNA WISH time course for *Shh* (cyan) and *Sp7* (dark purple) between E12.5 and E15.5. (a) Expression of *Sp7* in committed and differentiating osteoblasts delineates the growth dynamics of individual skeletal anlagen and *Shh* expression in rugae provides a temporally ordered set of A-P landmarks (regions in dashed boxes

539 enlarged below). (b) Summary model of skeletal growth dynamics during midfacial outgrowth. Growth of the
540 premaxilla (yellow) and palatine (pale blue) anlagen towards their characteristic shape occurs largely at the site of
541 initial specification. Following initial specification external to the oral cavity, the maxilla (purple) grows into the
542 anterior of the anterior secondary palate (black dashed arrows) towards the position of ruga 1 (red arrowhead) and
543 palatine as expansion of the anterior secondary palate (double headed red arrow) separates the primary and posterior
544 secondary palate. (c) Summary of the position of epithelial landmarks (see also Fig. 2) selected to capture segmental
545 growth dynamics of the primary palate (yellow) and anterior secondary palate (purple) and posterior secondary
546 palate (pale blue) during midfacial outgrowth. Abbreviations: maxilla (mx), palatine (p), premaxilla (pmx),
547 pterygoid (ptg), palatal process of the maxilla (ppmx), palatal process of the palatine (ppp)
548

549 In contrast, ruga 1 and the palatine anlage initially formed at the E11.5 anterior extent of
550 the secondary palate and maintained their proximity to each other throughout palatal
551 development even as they were displaced posteriorly between E11.5 and E15.5 (Fig. 7a). The
552 palatine and pterygoid bones later formed within the portion of the secondary palate that was
553 already present at the onset of secondary palate morphogenesis. These results indicated that the
554 posterior portion of the secondary palate and its associated anlage were present at the E11.5
555 onset of secondary palate morphogenesis, while the anterior secondary palate and associated
556 anlage did not contribute substantially to the secondary palate until later (Fig. 7b). The
557 combination of these morphogenetic results indicated that the meeting of the maxilla and
558 palatine anlagen was achieved predominantly by posterior growth of the maxilla towards the
559 palatine, which was itself being displaced posteriorly by anterior secondary palate elongation. By
560 E15.5, the maxilla and palatine anlagen met to form the maxillary-palatine suture subjacent to
561 ruga 1 (see also Supporting Fig. 1).
562 Our results collectively revealed that the segmental relationship between three palatal
563 regions and associated bone anlagen was already present at the onset of palatal morphogenesis.

564 Additionally, these results highlighted the previously unappreciated correlation of maxillary
565 growth to rugae formation as well as the greater proportional expansion of the anterior secondary
566 palate between E11.5 and E15.5 (summarized in Fig 7C). Based upon the spatial growth and
567 differential A-P dynamics revealed by our marker analysis, we defined a set of surface
568 landmarks intended to quantify the baseline characteristics and segmental differences in A-P
569 tissue domains underlying midfacial growth, within the context of overall midfacial elongation.
570

571 **Interstrain Comparisons of Facial and Palatal Growth**

572 Based on our findings that each upper jaw bone developed within one of the three palatal
573 segments and these segments contributed somewhat independently to midfacial A-P elongation,
574 we hypothesized that early differences in the proportional growth of the three palatal segments
575 produces strain specific differences in the contributions of specific bones to upper jaw length. If
576 true, previously identified differences in adult upper jaw morphology should be present by the
577 end of the critical embryonic A-P elongation period (i.e., by E15.5). We completed a
578 morphometric comparison of C57, NOD, and PWK strain embryonic midfacial shapes and a
579 comparison of proportional palatal segment lengths across embryonic and postnatal stages (Fig.
580 8) based on the direct relationship between segmental borders identified in the epithelial surfaces
581 and the specific bones that develop within the palatal segments.
582

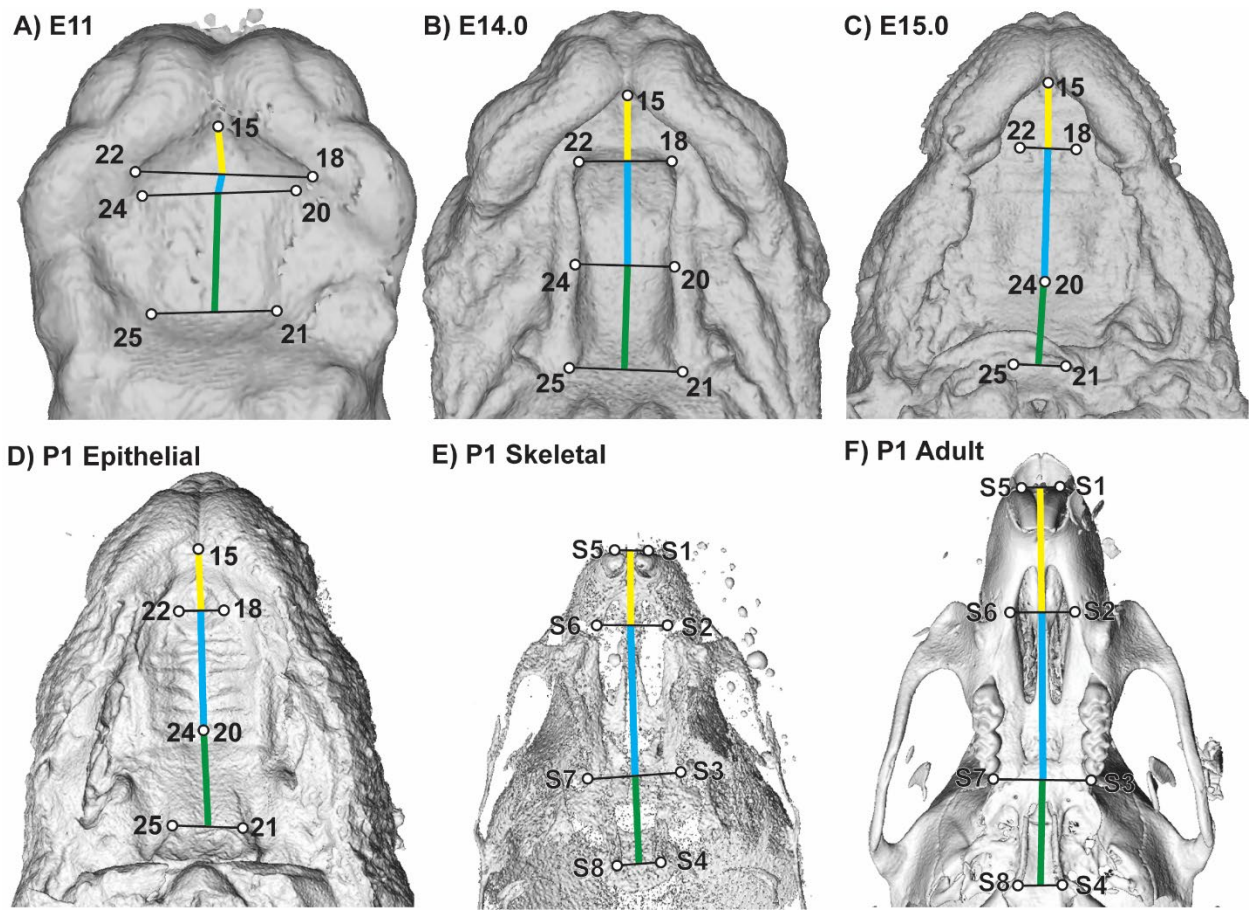

Figure 8 – Palate segment length measurements – Identification of landmarks used to estimate midline lengths of the primary palate (yellow), anterior secondary palate (blue), and posterior secondary palate (green) on (a) E11.0, (b) E14.0, (c) E15.0, (d) P1 epithelial palatal surfaces, (e) P1 skeletal surfaces, and (f) adult skeletal surfaces. See also Supporting Tables 1 and 2.

Since there is known variation in the speed of development between mouse strains and within litters, we standardized our cross-strain ontogenetic analysis by embryonic developmental age rather than gestational age. Limb bud outline-based developmental ages correlated strongly with the number of days after plug identification for each measured strain. Though the correlation coefficients for C57 mice (0.98), NOD (0.93) and PWK (0.90) were high, there was a larger difference between limb age estimates and copulatory plug-based estimates of embryonic

age for our PWK samples. The C57 specimen limb-based developmental ages were an average of 0.26 days younger than our copulatory plug estimates, while NOD and PWK limb ages were an average of 0.30 days and 1.09 days younger, respectively. The major divergence for PWK was likely driven by a slower speed of embryonic development in this wild-derived strain compared to the two common lab strains (Murray et al., 2010). Even so, standardization by developmental age should allow for improved direct comparisons between all strains.

We compared the midfacial shape of NOD and PWK specimens with C57 specimens along the principal axes of facial shape variation. This comparison indicated that mice with similar limb-based developmental age estimates tended to fall near each other along the first and second principal components, regardless of strain. As these axes represented 82% of facial shape variance across our sample, all mouse strains displayed major similarities in ontogenetic shape change across this period (Supporting Fig. 2A). However, across ontogenetic time (as represented by PC1 score) NOD and PWK specimens had significantly lower PC3 values compared to the C57 baseline (Fig. 9b). PWK specimens also had significantly lower PC4 values (Fig. 9c).

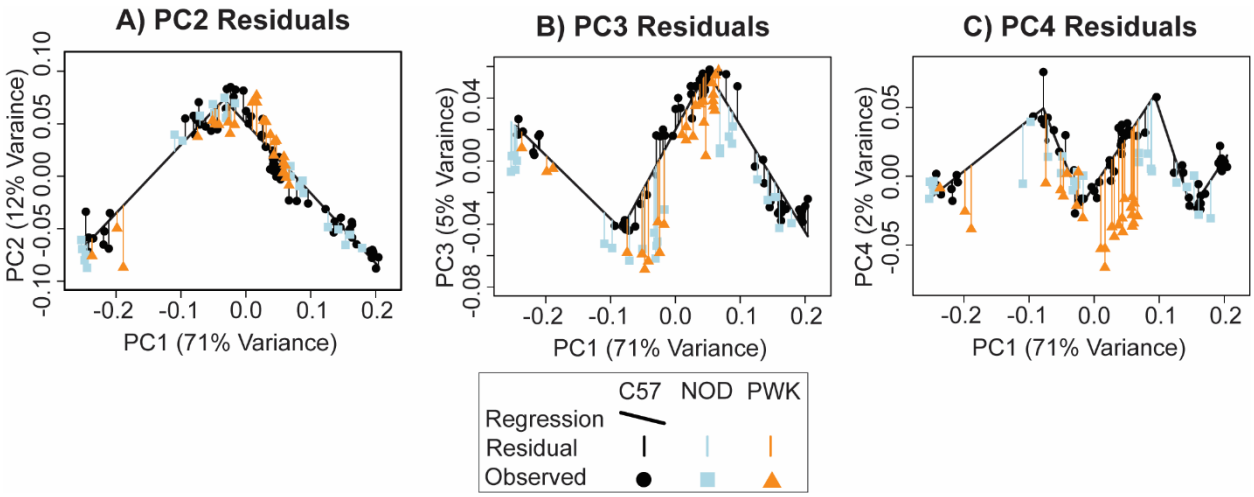

Figure 9 – Specimen PC score residuals – The principal component (PC) score residuals for each specimen, relative to the scores predicted from C57 strain specific segmented linear regressions of (a) PC2, (b) PC3, and (c) PC4 on the

613 specimen's PC1 score. In this way, the C57 facial shape growth trajectory serves as a baseline with which to
614 compare the shape of NOD and PWK specimens, based on the fact that the PC1 axis is strongly associated with
615 facial shape ontogeny from developmental age E11 to E15.
616
617 We visualized how these identified significant differences in PC3 or PC4 scores were
618 reflected within facial and palatal morphology by comparing shapes represented at the minimum
619 and maximum end of these major shape axes (Fig. 10). A minimum PC3 score was associated
620 with the two nostril landmarks (LM7 & 8) being relatively distant in the superior/inferior and
621 lateral directions. Lower PC3 score was also associated with relative proximity of the posterior
622 whisker margin (LM6) to the anterior canthus (LM4) (Fig. 10h). Within the palate, lower PC3
623 scores were associated with a relatively medial anterior secondary palatal shelf, suggesting more
624 medial palatal outgrowth (proportional to overall palatal length) at a given developmental stage
625 (Fig. 10b). The superior-inferior position of the palatal landmarks indicated that the secondary
626 palate was more highly angled (less flat) for specimens with low PC3 scores (Fig. 10e). Because
627 of their generally lower PC3 scores, we anticipated more vertical nostrils in NOD and PWK mice
628 with more highly angled palatal shelves in greater medial proximity to each other, when
629 compared to C57 mice within a given developmental age.

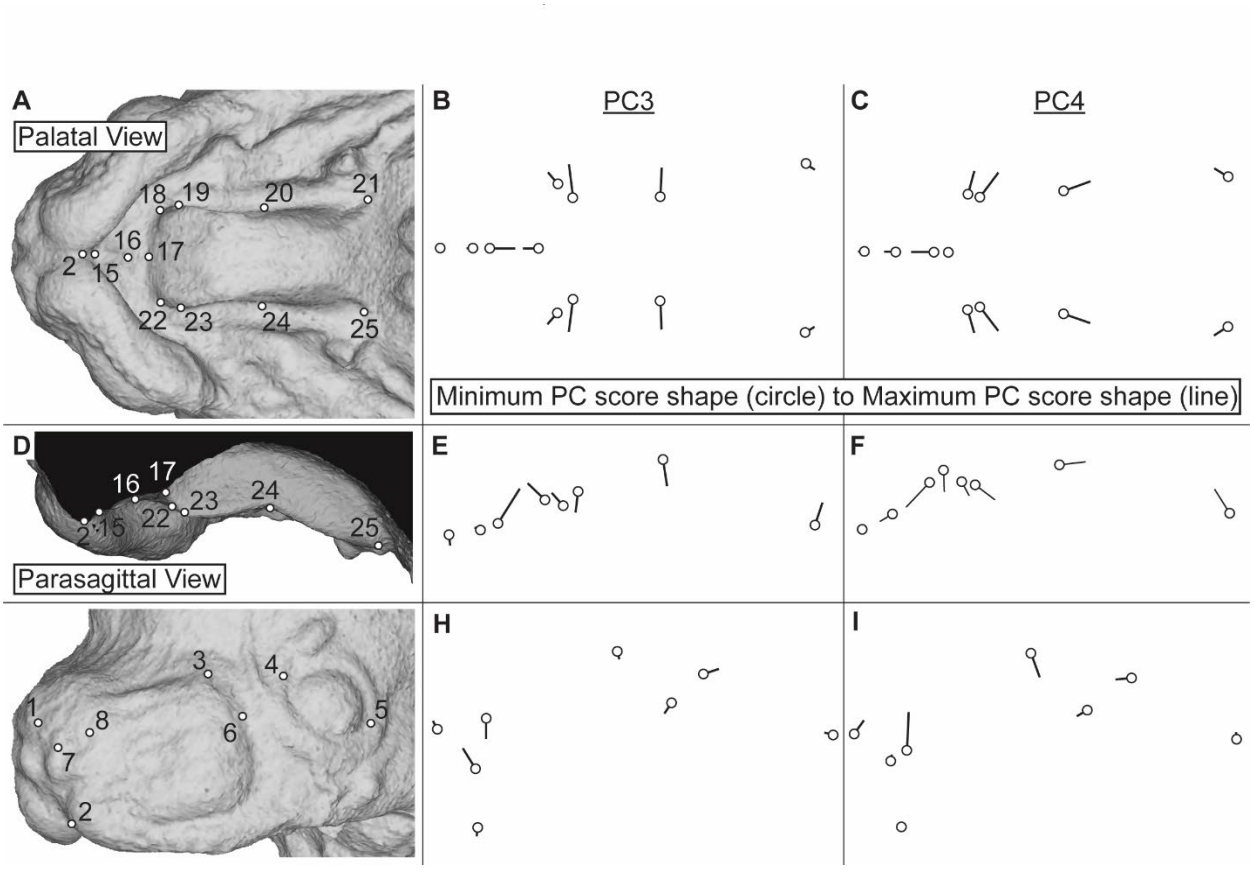

Figure 10 – Facial shape variation associated with PC3 and PC4 – Representation of the pattern of shape variation associated with the third major axis and fourth major axis of embryonic facial/palatal shape variation, from (a-c) palatal, (d-f) parasagittal, and (g-i) facial views. Superficial tissue landmarks are identified on an example E14.5 specimen to assist with interpretation of the landmark vectors that represent differences in minimum (circle) and maximum (end of line) PC scores. See Supporting Fig. 2 for a plot of embryonic specimens along these major axes of embryonic shape variation.

A minimum PC4 score was associated with the whole nasal region (LM1, LM8) being positioned more inferiorly and the posterior edge of the whisker region (LM3, LM6) more superiorly when compared to the other facial and palatal features (Fig. 10i, Supporting Fig. 4). Within the palate, a low PC4 score was associated with a relatively anterior location of ruga 1 between anterior and posterior secondary palate (LM20 & 24) and a relatively posterior position

643 of the posterior edge of the posterior secondary palate (LM21 & 25 within Fig. 10c). Low PC4
644 scores were also associated with more medially positioned anterior secondary palate landmarks
645 that are closer to the boundary with the primary palate. Because of their generally lower PC4
646 scores, this suggested that PWK embryos display a relatively low superior nasal region, a
647 medially expanded anterior secondary palatal shelf with a relatively short anterior secondary
648 palate and relatively long posterior secondary palate, when comparisons are made within a given
649 developmental age.

650 A comparison of embryonic palatal segment lengths (Fig. 8a-c) across C57, NOD and
651 PWK samples indicated that all three mouse strains display parallel ontogenetic changes 1) in
652 overall palatal length and 2) in the proportional contributions of palatal regions to overall palatal
653 length during the period of early palatal morphogenesis (Fig. 11). However, comparisons of
654 regression residuals of proportional segment length versus facial shape PC1 score (as a proxy for
655 developmental age) indicated small but significant differences in palatal segment proportions
656 between mouse strains. The NOD and PWK primary palate proportional length values were
657 significantly lower than for C57 (p-values: 0.012 (NOD vs C57), <0.001 (PWK vs C57)) (Fig.
658 12a), while they also had significantly higher posterior secondary palate values than C57 (p-
659 values <0.001) (Fig. 12c). This indicated that the primary palate contributed relatively less and
660 the posterior secondary palate contributed proportionally more to total embryonic palate length
661 in these two mouse strains, although visual assessment suggested these differences do not occur
662 at the earliest measured developmental ages (Fig. 11b). Significantly lower anterior secondary
663 palate values for NOD and PWK (p-values: 0.029 (NOD vs C57), 0.023 (PWK vs C57) indicated
664 that the anterior secondary palate represented a lower proportion of the total palate length within
665 these strains (Fig. 12b), although these differences seemed less pronounced than those noted for

666 the other two segments (Fig. 11b). Taken together, these general trends suggested that C57 mice
667 had proportionally longer primary palates and proportionally shorter posterior secondary palates
668 than NOD and PWK mice, with a trend towards longer anterior secondary palates by the time of
669 medial palatal shelf fusion (Fig. 12).
670

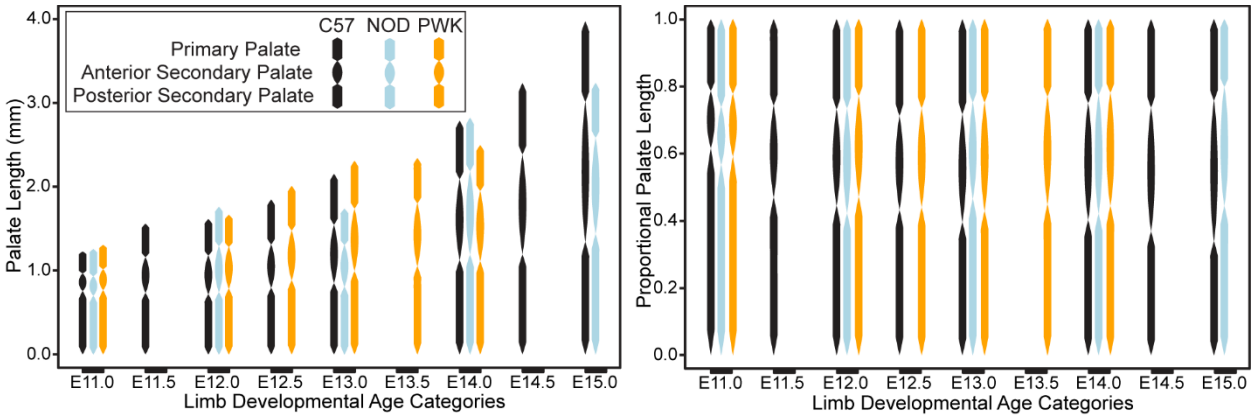

671

672 Figure 11 – Embryonic palate segment length across ontogeny – The midline projected strain-specific mean lengths
673 of the primary palate, anterior secondary palate, and posterior secondary palate, presented for each limb-based
674 developmental stage category (E11-E15). Raw length values (in millimeters) are presented on the left, while palatal
675 segment length relative to overall midline palate length are presented on the right.
676

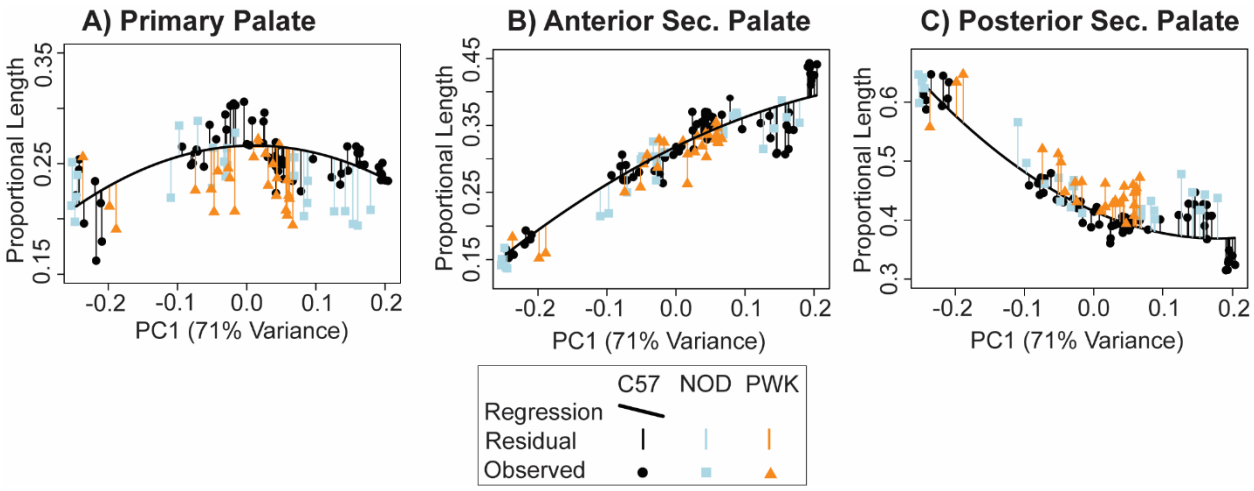

Figure 12 - Specimen palate segment length residuals – The proportional contributions of each palate length segment (shapes), as compared to the proportional contributions predicted from C57 strain specific linear regressions (curved lines) of proportional (a) primary palate, (b) anterior secondary palate, and (c) posterior secondary palate midline lengths versus the specimen's PC1 score. Vertical lines represent the residual of each specimen from C57 regression. In this way, the C57 palatal segment growth trajectory serves as a baseline that NOD and PWK specimens were compared to, based on the fact that the PC1 axis is strongly associated with facial shape ontogeny from E11 to E15.

Interstrain Comparisons of Postnatal Palatal Segments

We compared C57 and NOD proportional palatal segment lengths at P1 based on epithelial surface landmarks and skeletal landmarks of associated bony elements. Based on the P1 epithelial surface landmarks (Fig. 8d), C57 had a proportionally shorter anterior secondary palate and a proportionally longer posterior secondary palate (p-values <0.01) than NOD (Fig. 13; Table 2). This differed from the embryonic pattern where C57 specimens generally displayed proportionally shorter posterior secondary palates than NOD specimens. The significant differences in epithelially-measured proportional segment contributions between NOD and C57 mice at P1 appeared largely based on differences in the measured length (in mm) of the posterior secondary palate (Fig. 13).

Table 2 – Average proportional palatal segment lengths for postnatal specimens, presented as percentages of total palatal length.

	C57			NOD			PWK
	P1 epithelial	P1 bone	Adult bone	P1 epithelial	P1 bone	Adult bone	Adult bone
Primary Palate / Premaxilla	18.4%	23.3%	32.4%	19.7%	24.4%	31.7%	30.7%
Ant. Sec. Palate / Maxilla	45.7%	47.5%	39.9%	49.5%	47.4%	41.8%	42.8%
Post. Sec. Palate / Palatine & Pterygoid	35.9%	29.2%	27.7%	30.8%	28.3%	26.5%	26.5%

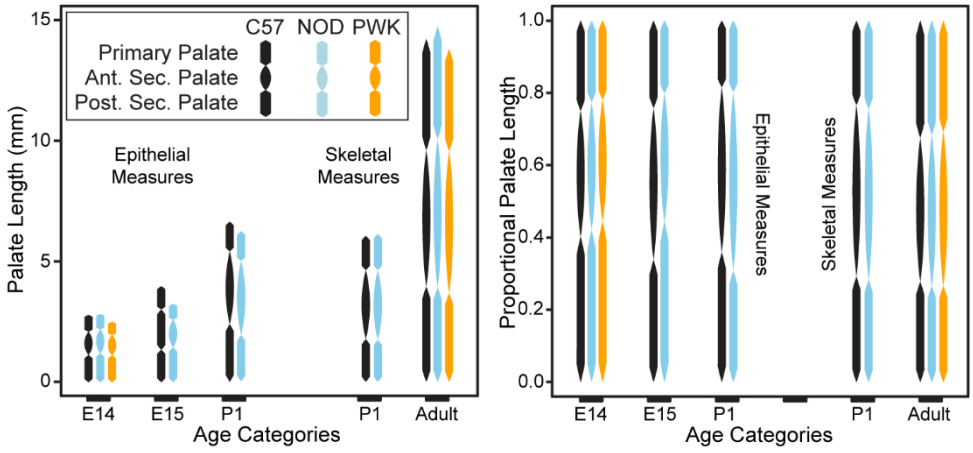

Figure 13 – Interstrain comparisons of palate segment lengths in older specimen – The midline projected strain-specific mean lengths of the primary palate, anterior secondary palate, and posterior secondary palate, based on epithelial landmark measures for limb based developmental stages E14 and E15, as well as for P1 specimens. Analogous length measures of primary palate derived premaxilla, anterior secondary palate derived maxilla, and posterior secondary palate derived palatine/pterygoid bones are presented for P1 and adult specimens. Raw length values (in millimeters) are presented on the left, while palatal segment length relative to overall midline palate length are presented on the right.

709 A comparison of proportional palatal bone lengths in P1 samples (Fig. 8e) indicated that
710 C57 has a proportionally shorter premaxilla (associated with primary palate) and proportionally
711 longer palatine/pterygoid bones (associated with posterior secondary palate) (p-values <0.01)
712 than NOD (Fig. 13; Table 2). A similar comparison of proportional palatal bone lengths (Fig. 8f)
713 in 8-12 week old adult specimens of all three strains revealed that the premaxillary (primary
714 palate) contribution to total palate length is significantly lower in PWK (p-value: < 0.001) and
715 NOD (p-value: 0.044) compared to C57, with the opposite true for the maxillary (anterior
716 secondary palate) portion of the palate (p-values: < 0.001) (Fig. 13). The palatine/pterygoid
717 (posterior secondary palate) portion was proportionally shorter in PWK and NOD when
718 compared to C57 (p-values: < 0.001) (Fig. 13). The PWK average proportional measures of
719 premaxilla and maxilla showed a more extreme divergence from C57 than in the NOD mouse
720 comparison.
721 Overall, there were some ontogenetic changes related to strain differences for
722 proportional palatal segment lengths from the embryonic period to P1 and then again between P1
723 and adulthood. NOD and C57 showed parallel postnatal changes in palatal bone contributions
724 across the postnatal period, where the posterior secondary palate contribution remained fairly
725 stable (~27-29%), but the primary palate contribution increased from ~24% to ~32% and the
726 anterior secondary palate contribution decreased from ~47% to ~40-42% (Fig. 13; Table 2).
727 During the postnatal period, the entire mouse and its palate grew substantially, but premaxilla
728 growth contributed more than the maxilla growth to overall postnatal palatal elongation.
729 Although the A-P growth of the anterior secondary palate was a critical driver for midfacial
730 growth between E11.5 and E15.5, outgrowth of the premaxilla may have played a larger role in
731 postnatal midfacial outgrowth.

732

733 **Discussion**

734 We provided here a multifaceted illustration of normal murine midfacial growth
735 dynamics within the secondary palate and upper jaw bones during the earliest stages of palatal
736 growth, followed by subsequent changes in upper jaw bone proportions in newborn and adult
737 mice. By tracking the position of the RGZ, each palatal ruga, and palatal bone precursor
738 populations across the earliest phases of palatal A-P elongation, our results confirmed that the
739 first-formed palatal ruga, which sits at an important border of regulatory gene expression, also
740 represents a consistent morphological boundary between the presumptive maxilla of the anterior
741 secondary palate and the presumptive palatine and pterygoid bones of the posterior secondary
742 palate. The process of rugae morphogenesis is coupled to maxillary osteogenesis during anterior
743 secondary palate expansion. Also, from the time of its formation, ruga 1 represents the future
744 position of the maxillary-palatine suture.

745 We tested the hypothesis that proportional differences in the earliest embryonic phases of
746 palatal segment A-P elongation underlie strain-specific differences in the adult contributions of
747 the premaxilla, maxilla, and palatine/pterygoid bones to upper jaw length. While these early
748 morphogenetic processes are critical for normal midfacial outgrowth, our ontogenetic
749 comparison of epithelial and skeletal palatal anatomy across three mouse strains indicated that
750 adult-like strain-specific differences in upper jaw morphology are not present before or at birth.
751 However, the significant strain-specific differences that were identified during embryonic palatal
752 morphogenesis are a useful foundation for understanding the impact of background genetic
753 effects on facial shape and elongation.

754

755 **Normal Upper Jaw and Palatal Elongation**

756 Between mouse E11.5 and E15.5, as overall head size increases, the fused facial
757 prominences grow dramatically outward to form an elongated snout. It is well known that A-P
758 elongation of the palate is a necessary component of the integrated processes of midfacial
759 outgrowth. However, we previously lacked a detailed picture of the earliest spatiotemporal
760 dynamics of intramembranous skeletal specification and differentiation in the mammalian
761 midface. Our combined morphometric and whole mount gene expression analysis spanned the
762 period of secondary palate morphogenesis, providing a detailed description of early
763 intramembranous skeletal specification and differentiation within the context of the surrounding
764 palatal segments and rugae formation. This work indicated that the relationship between three
765 longitudinal palate segments and associated upper jaw bones was already established during the
766 earliest phases of palatal morphogenesis. These results also illustrated how differential growth of
767 the palatal segments contribute to overall palate length in mice and likely in other mammals.
768 While all three palatal segments elongated between E11.5 and E15.5, the proportional elongation
769 of the anterior secondary palate was notably more pronounced than that of the primary or
770 posterior secondary palate and was accompanied by rugae formation at the RGZ and elongation
771 of the maxillary bone primordium.

772 Our results verified that ruga 1 forms at an important gene expression boundary between
773 the anterior and posterior secondary palate. They also clarified previous hypotheses regarding the
774 anatomical relationship between the position of ruga 1, the hard verus soft palate, and the
775 maxillary-palatine suture (Pantalacci et al., 2008). Our results established that throughout palate
776 morphogenesis, ruga 1 represents a stable morphological boundary positioned at the future
777 maxillary-palatine suture and not the more posterior soft palate. Posteriorly, ruga 1 maintained a

778 position at the anterior edge of the palatine anlage as both are posteriorly displaced between
779 E11.5 and E15.5. This implied that at E11.5 the secondary palate was initially comprised of only
780 the posterior secondary palate domains that will give rise to the palatine and pterygoid bones.
781 Anterior to ruga 1, growth of the maxillary anlage into the secondary palate only occurred as
782 anterior secondary palate expansion displaced the original site of maxillary specification
783 anteriorly away from ruga 1. This suggested that cellular cues in the proximity of ruga 1 may
784 initially inhibit maxillary bone formation. Expansion of the palatal portion of the maxillary
785 anlage appeared uniquely coupled to dynamics within the RGZ of anterior secondary palate
786 elongation, meaning this critical period of RGZ associated morphogenesis likely plays a major
787 role in determining the proportional contribution of the maxilla to the upper jaw within a broad
788 evolutionary context.

789 Differences in the formation and anatomy of two major upper jaw sutures may also be
790 related to segmental differences in early bone growth. The premaxilla and maxilla were specified
791 in adjacent tissue domains and maintained close apposition throughout palate morphogenesis,
792 suggesting equal contributions to the formation of the premaxillary-maxillary suture. Conversely,
793 the palatal portion of the maxilla grew posteriorly towards the palatine anlage at rugae 1,
794 suggesting that maxillary growth (and likely RGZ dynamics) played a larger role than palatine
795 growth in determining maxillary-palatine suture position. Different growth dynamics at these
796 sutures may lead to a more vertical premaxillary-maxillary suture versus a more oblique
797 maxillary-palatine suture with substantial A-P overlap of the maxilla and palatine bones. Suture
798 formation also provides a critical niche for facial skeletal progenitors (Zhao et al., 2015). Thus, it
799 is possible that early differences in segmental contributions to palate and upper jaw sutures may
800 also contribute to differences in postnatal dynamics of midfacial growth and remodeling (Enlow

801 and Bang, 1965; Kurihara et al., 1980; Sarnat, 1997; Martinez-Maza et al., 2013; Vora et al.,
802 2015; Maga, 2016). Further support for this hypothesis comes from recent work that showed the
803 widespread presence of Gli1+ mesenchymal stem cells and nascent bone formation (via calcein
804 labeling) within the center of the adult maxillary-palatine suture and also in the maxillary bone,
805 but a lack of stem cells and only sparse bone formation in the palatine bone (Luo et al., 2019).
806 Given the established role of calvarial sutures in directing bone growth of the skull, further
807 investigation of osteoprogenitor dynamics during premaxillary-maxillary and maxillary-palatine
808 suture formation is warranted.
809
810 **Interstrain Palatal Growth Comparison**
811 Our data illustrated 1) direct early associations between palatal segments and upper jaw
812 bones morphogenesis and 2) that anterior secondary palate growth makes a central contribution
813 towards total palatal elongation. This suggested a model where changes in embryonic A-P
814 growth of the anterior secondary palate at the RGZ may produce the range of prognathism
815 observed amongst mammals (Young et al., 2014). Given that A-P growth of the anterior
816 secondary palate was associated with rugae formation, support for this mechanism is further
817 strengthened by the fact that flat faced humans typically have 3-6 palatal rugae (Hauser et al.,
818 1989; Jayasankar et al., 2016), mice have 8-9 rugae (Peterkova et al., 1987), and prognathic pigs
819 have 20-25 rugae (Tonge and McCance, 1965). Based on this potential evo-devo relationship, we
820 hypothesized that intra-species differences in the contribution of individual bones to upper jaw
821 length would be produced by strain-specific differences in early embryonic A-P palatal segment
822 elongation. Based on previously reported adult phenotypes (Percival et al., 2016), we
823 hypothesized that C57 strain mice would have a relatively long primary palate and relatively

824 short anterior secondary palate by E15, while NOD and PWK mice would display the opposite
825 phenotype.

826 Although patterns of embryonic and postnatal palatal growth were broadly similar across
827 our three inbred mouse strains (Figs. 11 & 13), we identified significant strain-associated
828 differences in facial shape and palatal segment length. Embryonic facial shape differences (Figs.
829 4, 9, & 10; Table 2), as identified along major axes of variation, may represent more exaggerated
830 versions of normal ontogenetic shifts in the relationship of various facial structures or shifts in
831 the relative timing of normal developmental events occurring within different parts of the face.
832 Significant strain-specific differences in palatal segments proportions were identified across the
833 embryonic samples, with NOD and PWK mice having proportionally longer posterior secondary
834 palates and shorter primary palates than C57 mice. This result broadly matched our hypothesis
835 that embryonic C57 would have a relatively long primary palate, although without support for
836 initially predicted differences in anterior secondary palate proportions. Therefore, these results
837 demonstrated that there were significant embryonic differences in palatal proportions between
838 the strains, but they do not coincide with the differences observed in adults.

839 The results also indicated that differences in proportional segment lengths between NOD
840 and C57 did not remain consistent between the embryonic, neonatal (P1), and adult specimens.
841 At P1, NOD had a relatively short posterior secondary palate (i.e. palatine and pterygoid)
842 compared to C57, based on epithelial and skeletal measures. NOD also displayed a relatively
843 long anterior secondary palate based on epithelial measures and relatively long premaxilla (i.e.
844 primary palate) based on skeletal measures. This indicated a swap in proportional contributions
845 for primary palate and posterior secondary palate between E15 and P1. Strain-specific
846 premaxillary proportions flipped again between P1 and adult measurements.

847 Although changes within the RGZ growth dynamics of anterior secondary palate growth
848 may be critical for major species-specific differences in prognathism, our results did not support
849 the idea that this mechanism is responsible for the adult intraspecies differences in upper jaw
850 morphology between our mouse strains. This may indicate that later prenatal (after E15) and
851 postnatal growth processes play a major role in determining adult upper jaw bone proportions.
852 Our results suggested that variation in postnatal growth of the primary palate derived premaxilla
853 contributed more to postnatal elongation of the upper jaw than growth of the other palatal
854 segments did. A larger sample of later embryonic ages (i.e., between E15.5 and P0) would allow
855 us to determine when the initial NOD pattern of short primary and long posterior secondary
856 palate changes to a pattern of long primary and short posterior secondary palate by P1.
857
858 **Concluding Statement**
859 Our multifaceted illustration of normal midfacial growth dynamics confirmed a one-to-
860 one relationship between palatal segments and upper jaw bones during the earliest stages of
861 palatal growth, suggesting that the first formed ruga represents a consistent morphological
862 boundary between anterior and posterior secondary palate bone precursors, being found at the
863 future maxillary-palatine suture. Our results also indicated that interactions at the RGZ
864 simultaneously drives rugae formation and elongation of the maxillary bone primordium within
865 the anterior secondary palate, which more than doubles in length prior to palatal shelf fusion.
866 Although it is likely that RGZ-driven A-P growth of the anterior secondary palate contributes to
867 evolutionary changes in facial upper jaw morphology, this process was not solely responsible for
868 the subtle strain-specific upper jaw bone proportions measured across three inbred mouse strains.
869 However, significant strain-specific differences in early palatal segment elongation provide a

useful foundation for understanding the impact of background genetic effects on facial morphogenesis. Our multifaceted analysis of ontogenetic trends in palatal and facial elongation provides a novel contextual framework and developmental perspective within which to evaluate the impact of both non-pathogenic and pathogenic genetic differences on midfacial growth and differentiation.

Acknowledgements

We are indebted to Benedikt Hallgrímsson for the use of his laboratory for uCT and microscopy image collection. This work was supported by start-up funds to Christopher J. Percival from Stony Brook University; NIH/NIDCR R01 grant DE028753 and UCSF Chancellor Funds from Recruitment Package to Licia Selleri who supported the personnel and all the research completed in her lab for this study; and NIH/NIDCR F32 Fellowship DE026950 to Ian Welsh. The authors of this manuscript have no conflicts of interest to declare.

Data Availability Statement

µCT images, limb bud microcopy photographs, landmark coordinate data, and associated morphometric analysis R scripts will be made available publicly as a dataset within Dryad (https://doi.org/10.5061/dryad.ghx3ffbvb; Welsh et al., 2023) after publication of this manuscript within a peer-reviewed journal.

Supporting Information

Supporting Tables and Figures are found as a Supporting .pdf

Author Contributions

ICW contributed to study design, acquisition and interpretation of histological images, and drafting of the manuscript. MEF contributed to acquisition, analysis, and interpretation of morphometric data, and critical revision of the manuscript. DL contributed to the design of morphometric methods, acquisition of morphometric data, measurement and analysis of limb bud images, and critical revision of the manuscript. IM contributed to acquisition of µCT images, acquisition, measurement and analysis of limb bud images, and critical revision of the manuscript. KH contributed to mouse breeding, specimen collection, histological data collection, and critical revision of the manuscript. CJP contributed to study design, acquisition of µCT images, acquisition, analysis, and interpretation of morphometric data, and drafting of the manuscript.

References

Adams, D.C., Collyer, M.L., Kaliontzopoulou, A., 2020. geomorph: Software for geometric morphometric analyses. R package version 3.3.1.https://cran.r-project.org/package=geomorph

Boughner, J.C., Wat, S., Diewert, V.M., Young, N.M., Browder, L.W., Hallgrímsson, B., 2008. Short-faced mice and developmental interactions between the brain and the face. Journal of Anatomy 213, 646–662.

Bush, J.O., Jiang, R., 2012. Palatogenesis: morphogenetic and molecular mechanisms of secondary palate development. Development 139, 231–243.

Cignoni, P., Callieri, M., Corsini, M., Dellepiane, M., Ganovelli, F., Ranzuglia, G., 2008. Meshlab: an open-source mesh processing tool., in: Eurographics Italian Chapter Conference. pp. 129–136. https://doi.org/10.2312/LocalChapterEvents/ItalChap/ItalianChapConf2008/129-136

Cobb, S.N., O'Higgins, P., 2004. Hominins do not share a common postnatal facial ontogenetic shape trajectory. Journal of Experimental Zoology Part B: Molecular and Developmental Evolution 302, 302–321.

Collyer, M.L., Adams, D.C., 2018. RRPP: An R package for fitting linear models to high-dimensional data using residual randomization. Methods in Ecology and Evolution.

Dillon, S., Staines, K.A., Millán, J.L., Farquharson, C., 2019. How To Build a Bone: PHOSPHO1, Biomineralization, and Beyond. JBMR Plus 3, e10202. https://doi.org/10.1002/jbm4.10202

926 Economou, A.D., Ohazama, A., Porntaveetus, T., Sharpe, P.T., Kondo, S., Basson, M.A., et al.,
927 2012. Periodic stripe formation by a Turing mechanism operating at growth zones in the
928 mammalian palate. Nat Genet 44, 348–351. https://doi.org/10.1038/ng.1090
929 Enlow, D.H., Bang, S., 1965. Growth and remodeling of the human maxilla. Am J Orthod 51,
930 446–464. https://doi.org/10.1016/0002-9416(65)90242-3
931 Fedorov, A., Beichel, R., Kalpathy-Cramer, J., Finet, J., Fillion-Robin, J.-C., Pujol, S., et. al.,
932 2012. 3D Slicer as an image computing platform for the Quantitative Imaging Network.
933 Magnetic Resonance Imaging 30, 1323–1341. https://doi.org/10.1016/j.mri.2012.05.001
934 Fish, J.L., 2019. Evolvability of the vertebrate craniofacial skeleton. Semin Cell Dev Biol 91,
935 13–22. https://doi.org/10.1016/j.semcdb.2017.12.004
936 Galea, G.L., Zein, M.R., Allen, S., Francis-West, P., 2021. Making and shaping endochondral
937 and intramembranous bones. Dev Dyn 250, 414–449. https://doi.org/10.1002/dvdy.278
938 Geyer, S.H., Mohun, T.J., Weninger, W.J., 2009. Visualizing vertebrate embryos with episcopic
939 3D imaging techniques. ScientificWorldJournal 9, 1423–1437.
940 https://doi.org/10.1100/tsw.2009.154
941 Hall, J., Jheon, A.H., Ealba, E.L., Eames, B.F., Butcher, K.D., Mak, S.-S., et. al., 2014.
942 Evolution of a developmental mechanism: Species-specific regulation of the cell cycle
943 and the timing of events during craniofacial osteogenesis. Dev Biol 385, 380–395.
944 https://doi.org/10.1016/j.ydbio.2013.11.011
945 Hallgrímsson, B., Jamniczky, H., Young, N.M., Rolian, C., Parsons, T.E., Boughner, J.C., et. al.,
946 2009. Deciphering the Palimpsest: Studying the Relationship between Morphological
947 Integration and Phenotypic Covariation. Evolutionary Biology 36, 355–376.
948 Hammond, N.L., Dixon, M.J., 2022. Revisiting the embryogenesis of lip and palate
949 development. Oral Dis 28, 1306–1326. https://doi.org/10.1111/odi.14174
950 Hauser, G., Daponte, A., Roberts, M., 1989. Palatal rugae. Journal of Anatomy 165, 237–249.
951 Hilliard, S.A., Yu, L., Gu, S., Zhang, Z., Chen, Y.P., 2005. Regional regulation of palatal growth
952 and patterning along the anterior–posterior axis in mice. Journal of Anatomy 207, 655–
953 667. https://doi.org/10.1111/j.1469-7580.2005.00474.x
954 Hojo, H., Ohba, S., 2022. Sp7 Action in the Skeleton: Its Mode of Action, Functions, and
955 Relevance to Skeletal Diseases. Int J Mol Sci 23, 5647.
956 https://doi.org/10.3390/ijms23105647
957 Jayasankar, P., Banker, A., Bhattacharya, A., Gandhi, R., Patel, N., Parikh, S., 2016. Quantitative
958 and qualitative analysis of palatal rugae patterns in Gujarati population: A retrospective,
959 cross-sectional study. J Forensic Dent Sci 8, 126. https://doi.org/10.4103/0975-
960 1475.195110
961 Kaucka, M., Petersen, J., Tesarova, M., Szarowska, B., Kastriti, M.E., Xie, M., et. al., 2018.
962 Signals from the brain and olfactory epithelium control shaping of the mammalian nasal
963 capsule cartilage. Elife 7, e34465. https://doi.org/10.7554/eLife.34465
964 Kawasaki, M., Kawasaki, K., Meguro, F., Yamada, A., Ishikawa, R., Porntaveetus, T., et. al.,
965 2018. Lrp4/Wise regulates palatal rugae development through Turing-type reaction-
966 diffusion mechanisms. PLoS One 13, e0204126.
967 https://doi.org/10.1371/journal.pone.0204126
968 Kundrát, M., Coria, R.A., Manning, T.W., Snitting, D., Chiappe, L.M., Nudds, J., et. al., 2020.
969 Specialized Craniofacial Anatomy of a Titanosaurian Embryo from Argentina. Current
970 Biology 30, 4263-4269.e2. https://doi.org/10.1016/j.cub.2020.07.091

971 Kurihara, S., Enlow, D.H., Rangel, R.D., 1980. Remodeling reversals in anterior parts of the
972 human mandible and maxilla. Angle Orthod 50, 98–106. https://doi.org/10.1043/0003-
973 3219(1980)050<0098:RRIAPO>2.0.CO;2
974 Lee, S.-H., Bédard, O., Buchtová, M., Fu, K., Richman, J.M., 2004. A new origin for the
975 maxillary jaw. Developmental biology 276, 207–224.
976 Leigh, S.R., 2006. Cranial ontogeny of Papio baboons (Papio hamadryas). American Journal of
977 Physical Anthropology 130, 71–84. https://doi.org/10.1002/ajpa.20319
978 Li, Q., Ding, J., 2007. Gene expression analysis reveals that formation of the mouse anterior
979 secondary palate involves recruitment of cells from the posterior side. Int. J. Dev. Biol.
980 51, 167–172.
981 Luo, W., Yi, Y., Jing, D., Zhang, S., Men, Y., Ge, W.-P., et. al., 2019. Investigation of Postnatal
982 Craniofacial Bone Development with Tissue Clearing-Based Three-Dimensional
983 Imaging. Stem Cells and Development 28, 1310–1321.
984 https://doi.org/10.1089/scd.2019.0104
985 Maga, A.M., 2016. Postnatal Development of the Craniofacial Skeleton in Male C57BL/6J Mice.
986 J Am Assoc Lab Anim Sci 55, 131–136.
987 Martinez-Maza, C., Rosas, A., Nieto-Díaz, M., 2013. Postnatal changes in the growth dynamics
988 of the human face revealed from bone modelling patterns. J Anat 223, 228–241.
989 https://doi.org/10.1111/joa.12075
990 Morris, Z.S., Abzhanov, A., 2021. Heading for higher ground: Developmental origins and
991 evolutionary diversification of the amniote face. Curr Top Dev Biol 141, 241–277.
992 https://doi.org/10.1016/bs.ctdb.2020.12.003
993 Murray, S.A., Morgan, J.L., Kane, C., Sharma, Y., Heffner, C.S., Lake, J., et. al., 2010. Mouse
994 Gestation Length Is Genetically Determined. PLoS ONE 5, e12418.
995 https://doi.org/10.1371/journal.pone.0012418
996 Musy, M., Flaherty, K., Raspopovic, J., Robert-Moreno, A., Richtsmeier, J.T., Sharpe, J., 2018.
997 A quantitative method for staging mouse embryos based on limb morphometry.
998 Development 145, 1–7.
999 Okano, J., Suzuki, S., Shiota, K., 2006. Regional heterogeneity in the developing palate:
1000 morphological and molecular evidence for normal and abnormal palatogenesis.
1001 Congenital Anomalies 46, 49–54. https://doi.org/10.1111/j.1741-4520.2006.00103.x
1002 Palmer, A.R., Strobeck, C., 1986. Fluctuating Asymmetry: Measurement, Analysis, Patterns.
1003 Annu. Rev. Ecol. Syst. 17, 391–421.
1004 https://doi.org/10.1146/annurev.es.17.110186.002135
1005 Pantalacci, S., Prochazka, J., Martin, A., Rothova, M., Lambert, A., Bernard, L., et. al., 2008.
1006 Patterning of palatal rugae through sequential addition reveals an anterior/posterior
1007 boundary in palatal development. BMC Developmental Biology 8, 116.
1008 https://doi.org/10.1186/1471-213X-8-116
1009 Pauws, E., Hoshino, A., Bentley, L., Prajapati, S., Keller, C., Hammond, P., et. al., 2009.
1010 Tbx22null mice have a submucous cleft palate due to reduced palatal bone formation and
1011 also display ankyloglossia and choanal atresia phenotypes. Hum Mol Genet 18, 4171–
1012 4179. https://doi.org/10.1093/hmg/ddp368
1013 Percival, C.J., Liberton, D.K., Pardo-Manuel de Villena, F., Spritz, R., Marcucio, R.,
1014 Hallgrímsson, B., 2016. Genetics of murine craniofacial morphology: diallel analysis of
1015 the eight founders of the Collaborative Cross. Journal of Anatomy 228, 96–112.
1016 https://doi.org/10.1111/joa.12382

1017 Peterkova, R., Klepacek, I., Peterka, M., 1987. Prenatal development of rugae palatinae in mice:
1018 scanning electron microscopic and histologic studies. Journal of craniofacial genetics and
1019 developmental biology 7, 169–89.
1020 Ponce de León, M.S.P., Zollikofer, C.P.E., 2001. Neanderthal cranial ontogeny and its
1021 implications for late hominid diversity. Nature 412, 534–538.
1022 R Core Team, 2021. R: A language and environment for statistical computing. R Foundation for
1023 Statistical Computing, Vienna, Austria [WWW Document]. URL https://www.R-
1024 project.org/
1025 Sarnat, B.G., 1997. Some methods of assessing postnatal craniofaciodental growth: a
1026 retrospective of personal research. Cleft Palate Craniofac J 34, 159–172.
1027 https://doi.org/10.1597/1545-1569_1997_034_0159_smoapc_2.3.co_2
1028 Schneider, R.A., 2015. Regulation of Jaw Length During Development, Disease, and Evolution.
1029 Curr Top Dev Biol 115, 271–298. https://doi.org/10.1016/bs.ctdb.2015.08.002
1030 Selleri, L., Rijli, F.M., 2023. Shaping faces: genetic and epigenetic control of craniofacial
1031 morphogenesis. Nature Reviews Genetics 24, 610–626. https://doi.org/10.1038/s41576-
1032 023-00594-w
1033 Singleton, M., 2012. Postnatal Cranial Development in Papionin Primates: An Alternative Model
1034 for Hominin Evolutionary Development. Evolutionary Biology 39, 499–520.
1035 https://doi.org/10.1007/s11692-011-9153-4
1036 Smith, F.J., Percival, C.J., Young, N.M., Hu, D., Schneider, R.A., Marcucio, R.S., et. al., 2015.
1037 Divergence of craniofacial developmental trajectories among avian embryos.
1038 Developmental Dynamics. https://doi.org/10.1002/dvdy.24262
1039 Tonge, C.H., McCance, R.A., 1965. Severe undernutrition in growing and adult animals: 15. The
1040 mouth, jaws and teeth of pigs. British Journal of Nutrition 19, 361–372.
1041 https://doi.org/10.1079/BJN19650034
1042 Vora, S.R., Camci, E.D., Cox, T.C., 2015. Postnatal Ontogeny of the Cranial Base and
1043 Craniofacial Skeleton in Male C57BL/6J Mice: A Reference Standard for Quantitative
1044 Analysis. Front Physiol 6, 417. https://doi.org/10.3389/fphys.2015.00417
1045 Welsh, I.C., Feiler, M.E., Lipman, D., Mormile, I., Hansen, K., Percival, C.J., 2023. Palatal
1046 segment contributions to midfacial growth in three inbred mouse strains.
1047 https://doi.org/10.5061/dryad.ghx3ffbvb
1048 Welsh, I.C., Hagge-Greenberg, A., O'Brien, T.P., 2007. A dosage-dependent role for Spry2 in
1049 growth and patterning during palate development. Mechanisms of Development 124,
1050 746–761. https://doi.org/10.1016/j.mod.2007.06.007
1051 Welsh, I.C., Hart, J., Brown, J.M., Hansen, K., Rocha Marques, M., Aho, R.J., et. al., 2018. Pbx
1052 loss in cranial neural crest, unlike in epithelium, results in cleft palate only and a broader
1053 midface. Journal of Anatomy 233, 222–242. https://doi.org/10.1111/joa.12821
1054 Welsh, I.C., O'Brien, T.P., 2009. Signaling integration in the rugae growth zone directs
1055 sequential SHH signaling center formation during the rostral outgrowth of the palate.
1056 Developmental Biology 336, 53–67. https://doi.org/10.1016/j.ydbio.2009.09.028
1057 Wilson, R., McGuire, C., Mohun, T., DMDD Project, 2016. Deciphering the mechanisms of
1058 developmental disorders: phenotype analysis of embryos from mutant mouse lines.
1059 Nucleic Acids Res 44, D855-861. https://doi.org/10.1093/nar/gkv1138
1060 Woronowicz, K.C., Schneider, R.A., 2019. Molecular and cellular mechanisms underlying the
1061 evolution of form and function in the amniote jaw. EvoDevo 10, 17.
1062 https://doi.org/10.1186/s13227-019-0131-8

1063 Young, N.M., Hu, D., Lainoff, A.J., Smith, F.J., Diaz, R., Tucker, A.S., et. al., 2014. Embryonic
1064 bauplans and the developmental origins of facial diversity and constraint. Development
1065 141, 1059–1063. https://doi.org/10.1242/dev.099994
1066 Yu, K., Ornitz, D.M., 2011. Histomorphological study of palatal shelf elevation during murine
1067 secondary palate formation. Developmental Dynamics 240, 1737–1744.
1068 https://doi.org/10.1002/dvdy.22670
1069 Yu, L., Gu, S., Alappat, S., Song, Y., Yan, M., Zhang, X., et. al., 2005. Shox2-deficient mice
1070 exhibit a rare type of incomplete clefting of the secondary palate. Development 132,
1071 4397–4406. https://doi.org/10.1242/dev.02013
1072 Yuan, Y., Loh, Y.-H.E., Han, X., Feng, J., Ho, T.-V., He, J., et. al., 2020. Spatiotemporal cellular
1073 movement and fate decisions during first pharyngeal arch morphogenesis. Sci Adv 6,
1074 eabb0119. https://doi.org/10.1126/sciadv.abb0119
1075 Zelditch, M., Swiderski, D., Sheets, D.H., 2012. Geometric morphometrics for biologists: a
1076 primer, 2nd ed. Elsevier Academic Press, San Diego.
1077 Zhao, H., Feng, J., Ho, T.-V., Grimes, W., Urata, M., Chai, Y., 2015. The suture provides a niche
1078 for mesenchymal stem cells of craniofacial bones. Nat Cell Biol 17, 386–396.
1079 https://doi.org/10.1038/ncb3139
1080 Zumpano, M.P., Richtsmeier, J.T., 2003. Growth-related shape changes in the fetal craniofacial
1081 complex of humans (Homo sapiens) and pigtailed macaques (Macaca nemestrina): a 3D-
1082 CT comparative analysis. American Journal of Physical Anthropology 120, 339–351.